WIYN Open Cluster Study. LXXXII. Radial-velocity Measurements and Spectroscopic Binary Orbits in the Open Cluster NGC 7789

Andrew C. Nine[1] , Katelyn E. Milliman[1,2] , Robert D. Mathieu[1] , Aaron M. Geller[3,4] , Emily M. Leiner[1,3,7] ,
Imants Platais[5] , and Benjamin M. Tofflemire[1,6]

[1] Department of Astronomy, University of Wisconsin-Madison, 475 N. Charter St., Madison, WI 53706, USA; anine@astro.wisc.edu
[2] Department of Space Studies, American Public University, 111 W. Congress St., Charles Town, WV 25414, USA
[3] Center for Interdisciplinary Exploration and Research in Astrophysics (CIERA) and Department of Physics and Astronomy, Northwestern University, 1800 Sherman Ave., Evanston, IL 60208, USA
[4] Adler Planetarium, Department of Astronomy, 1300 S. Lake Shore Dr., Chicago, IL 60605, USA
[5] Department of Physics and Astronomy, Johns Hopkins University, 3400 N. Charles St., Baltimore, MD 21218, USA
[6] Department of Astronomy, University of Texas at Austin, 2515 Speedway, Stop C1400, Austin, TX 78712, USA
Received 2020 March 21; revised 2020 August 4; accepted 2020 August 5; published 2020 September 21

Abstract

We present an extensive time-series radial-velocity (RV) survey of stars in the rich open cluster NGC 7789 (1.6 Gyr, [Fe/H] = +0.02). The stellar sample lies within an 18′ circular radius from the cluster center (10 pc in projection, or about 2 core radii), and includes giants, red clump stars, blue stragglers, red stragglers, sub-subgiants, and main-sequence stars down to 1 mag below the turnoff. Our survey began in 2005 and comprises more than 9000 RV measurements from the Hydra Multi-Object Spectrograph on the WIYN 3.5 m telescope. We identify 624 likely cluster members and present the orbital solutions for 81 cluster binary stars with periods between 1.45 and 4200 days. From the main-sequence binary solutions we fit a circularization period of $7.2^{+0.6}_{-1.1}$ days. We calculate an incompleteness-corrected main-sequence binary frequency of 31% ± 4% for binaries with periods less than 10^4 days, similar to other WIYN Open Cluster Survey (WOCS) open clusters of all ages. We detect a blue straggler binary frequency of 33% ± 17%, consistent with the similarly aged open cluster NGC 6819. We also find one secure, rapidly rotating sub-subgiant and one red straggler candidate in our sample.

Unified Astronomy Thesaurus concepts: Binary stars (154); Spectroscopic binary stars (1557); Close binary stars (254)

Supporting material: machine-readable tables

1. Introduction

The WIYN Open Cluster Study (WOCS; Mathieu 2000) seeks to probe a wide variety of questions in stellar astrophysics by acquiring comprehensive photometric, astrometric, and spectroscopic data on a selected set of rich, nearby open clusters that span age and metallicity (150 Myr $\lesssim$ $t \lesssim$ 8 Gyr; $-0.4 \lesssim$ [Fe/H] $\lesssim$ +0.3). Within WOCS, extensive data have been combined and presented for M35 (150 Myr; Geller et al. 2010; Thompson et al. 2014; Leiner et al. 2015), NGC 6819 (2.5 Gyr; Platais et al. 2013; Yang et al. 2013; Milliman et al. 2014), M67 (4 Gyr; A. M. Geller et al. 2020, in preparation, and references therein), NGC 188 (7 Gyr; Sarajedini et al. 1999; Platais et al. 2003; Geller & Mathieu 2012), and NGC 6791 (8 Gyr; Platais et al. 2013; Tofflemire et al. 2014). These data have been the foundation for a wide array of scientific discoveries including insights into blue straggler star (BSS) formation (Geller & Mathieu 2011; Gosnell et al. 2015; Milliman et al. 2015; Leiner et al. 2019; Mathieu & Leiner 2019), an age-rotation relationship for cool stars (Meibom et al. 2015), open cluster sub-subgiants (Milliman et al. 2016; Geller et al. 2017a, 2017b; Leiner et al. 2017), and more (Sandquist et al. 2018; Deliyannis et al. 2019).

In this paper we introduce the stellar sample of the WOCS radial-velocity (RV) survey of NGC 7789 ($\alpha = 23^\mathrm{h}57^\mathrm{m}21\!\!\overset{\mathrm{s}}{.}6$, $\delta = +56°43'22''$ J2000). NGC 7789 is a well-populated, 1.6 Gyr (Gim et al. 1998b) open cluster at a distance of

2075 ± 4 pc (Cantat-Gaudin et al. 2018), with [Fe/H] = +0.02 ± 0.04 (Jacobson et al. 2011). Wu et al. (2009) measure a core radius of 8′.8 ± 0′.9 and determine a cluster mass between 5150 $M_\odot$ and 7710 $M_\odot$ depending on the measurement method used.

Photometric studies of NGC 7789 begin with Burbidge & Sandage (1958) and include the *VI* photometry of Gim et al. (1998b) as well as the variability surveys of Jahn et al. (1995), Mochejska & Kaluzny (1999), and Zhang et al. (2003). A proper-motion study of McNamara & Solomon (1981) focused on evolved stars in NGC 7789. Here, we adopt the astrometry of Gaia Data Release 2 (Gaia DR2; Gaia Collaboration et al. 2016, 2018a, 2018b). The use of Gaia DR2 allows the confident identification of cluster members based on their proper motions and parallaxes (Cantat-Gaudin et al. 2018; Gao 2018).

The bright giants in NGC 7789 have also been the target of many spectroscopic abundance studies including Pancino et al. (2010), Jacobson et al. (2011), and Overbeek et al. (2015). These abundance studies as well as the RV surveys of cluster giants done by Gim et al. (1998a) and Casamiquela et al. (2016) have provided one to several RV measurements for most of the evolved stars in NGC 7789. With this paper we provide a complete RV time-series survey from the most luminous stars down to ∼1 mag below the main-sequence turnoff. We also present the first comprehensive collection of spectroscopic binary orbit solutions for NGC 7789, and use these solutions for a first look at connections between binaries and the stellar population.

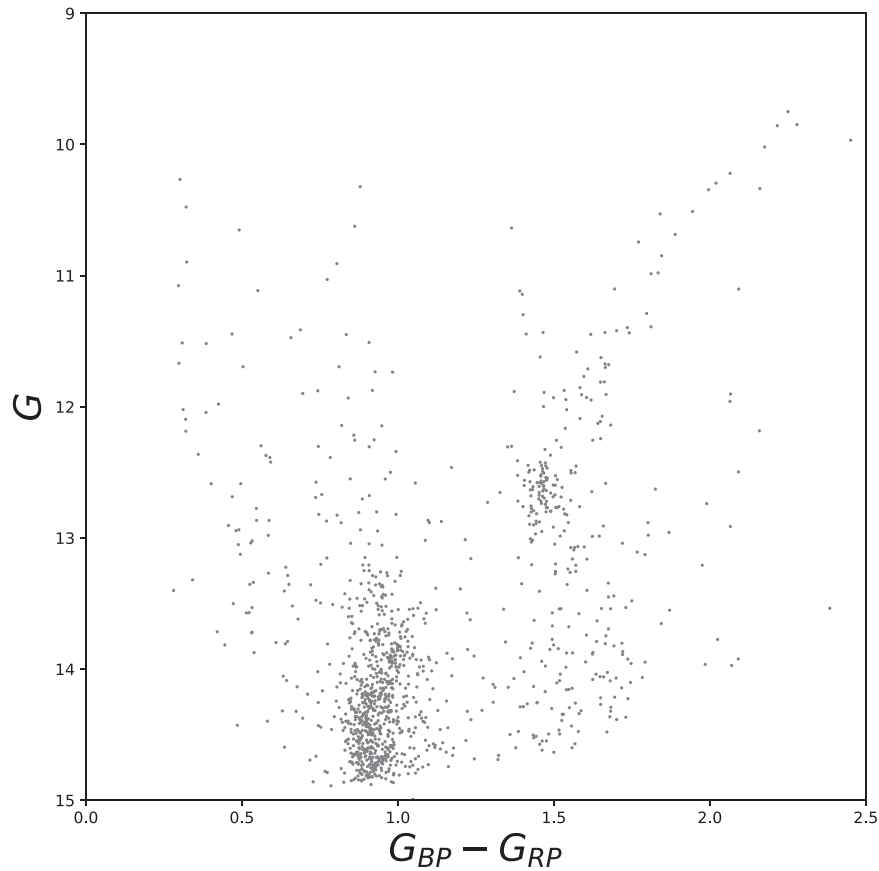[7] NSF Astronomy and Astrophysics Postdoctoral Fellow.

Figure 1. CMD of the NGC 7789 stars in our RV target sample based on the photometry of Gaia Collaboration et al. (2018b). The cluster's giant branch, red clump, and upper main sequence are clearly present, as well as a large number of BSS candidates.

2. Stellar Sample and Photometry

The stellar sample for NGC 7789 that is the basis for this paper includes 1206 stars. The sample was initially built from the extensive *VI* CCD photometry of Gim et al. (1998b). This photometry was obtained from the Dominion Astrophysical Observatory (DOA) 1.8 m Plaskett telescope and covers ∼18′ radius from the center of NGC 7789. The full photometry set has over 15,000 stars, is complete from $V \sim 10$ to $V \sim 21$, and has a V standard error under ∼0.01 mag down to our sample cutoff at $V = 15.0$. As in Milliman et al. (2014), we made selections in V and in $V - I$, such that $V < 15.0$ and that the stars brighter than this cutoff had a measured $V - I$ in Gim et al. (1998b). We applied these criteria in order to include the upper main sequence, red clump, giant branch, and BSS, as well as other alternative stellar evolution products in the cluster.

We then cross-matched this sample of stars with Gaia DR2 using TOPCAT (Taylor 2005). From our sample of 1206 stars, we were able to retrieve matches for 1204 stars using a tolerance in position of 1″. Of these, 1187 had full photometric and five-dimensional astrometric information. We use the proper motions to determine cluster memberships for our RV sample, discussed in detail in Section 6.3. The remaining 17 stars had insufficient proper-motion information for complete membership determination (Section 6.4). Out of these 17 stars, 6 are RV members (Section 6.2) and are classified as cluster members. We adopt the photometry of Gaia DR2 for the remainder of this paper. As shown in the color–magnitude diagram (CMD) of our sample (Figure 1), our study extends from $G \sim 10$ to $G \sim 15$, 1 mag below the main-sequence turnoff, and includes giant stars, a well-populated red clump, and a large number of BSS candidates.

3. WIYN Observations and Data Reduction

Our observations of NGC 7789 began in 2005 January using the Hydra Multi-Object Spectrograph (MOS; Barden et al. 1994) on the WIYN[8] 3.5 m telescope. Our spectra are typically taken in a wavelength range of ∼500 Å centered on 5125 Å which encompasses the Mg B triplet and a rich array of narrow metal lines. We conduct our observations at 11th order, which yields a spectral resolution of ∼15,000–20,000 with a dispersion of 0.13 Å/pix. More details on our observational setup can be found in Geller et al. (2008).

We follow the standard data acquisition and reduction procedures of the WOCS RV survey, also described in Geller et al. (2008). Briefly, for each configuration our data include one 200 s dome flat and two 300 s thorium-argon emission lamp spectra, one each before and after three science integrations. We use standard IRAF routines to bias subtract, dispersion correct, and extract each spectrum. We then flat-field, throughput correct, and subtract the sky from these spectra. In 2014 August we incorporated the L.A. Cosmic routine (van Dokkum 2001) for improved cosmic-ray rejection.

The goal of this study is to conduct time-series observations of evolved stars, stars on the upper main sequence, and stars on

---

[8] The WIYN 3.5 m Observatory is a joint facility of the University of Wisconsin–Madison, Indiana University, and the National Optical Astronomy Observatory.
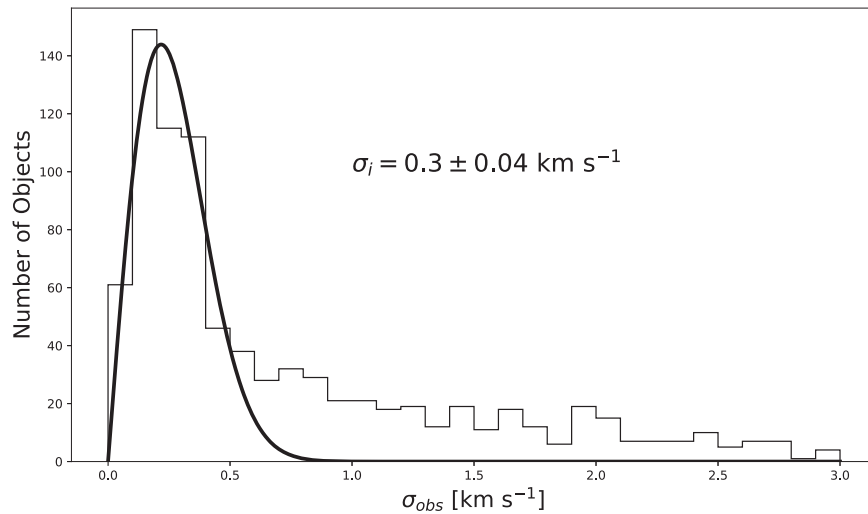
Figure 2. Histogram of the RV standard deviations from the first three observations of the narrow-lined stars in our sample. We overplot the best-fit χ^2 distribution function with a precision of 0.3 ± 0.04 km s^{-1}. The excesses above the theoretical distribution beginning at 0.5 km s^{-1} are velocity-variable stars.

Table 1
Radial-velocity Measurements

ID	HJD-2,400,000 (days)	RV_1 (km s^{-1})	Correlation Height$_1$	$O-C_1$ (km s^{-1})	RV_2 (km s^{-1})	Correlation Height$_2$	$O-C_2$ (km s^{-1})	Phase
7003								
	53720.7009	−95.5	0.41	−1.6	−12.5	0.29	−1.6	0.132
	54275.9141	−76.5	0.67	−0.9	−28.4	0.56	−0.9	0.261
	54676.9439	−58.7	0.85	…	…	…	…	…
	54683.9428	−39.4	0.77	−0.8	−69.1	0.72	−0.8	0.583
	54715.7860	−36.9	0.67	−2.0	−74.3	0.62	−2.0	0.622
	54723.8472	−25.6	0.78	−2.3	−86.2	0.65	−2.3	0.886
	54724.7236	−26.4	0.76	2.2	−79.3	0.63	2.2	0.915
	54747.8150	−28.8	0.81	1.9	−82.3	0.67	1.9	0.669
	54845.7016	−20.7	0.52	0.6	−91.0	0.34	0.6	0.865
	55018.7892	−52.9	0.80	…	…	…	…	…

(This table is available in its entirety in machine-readable form.)

alternative evolutionary tracks in order to detect binaries and determine their orbital properties. For each observing run we use a prioritization system described in Geller et al. (2008) that emphasizes high-amplitude velocity-variable, short-period binaries, followed by longer period binaries, binary candidates, and survey observations of remaining stars. For a complete orbital solution, we typically require a minimum of 12 RV measurements, as defined in Section 4, and that the best-fit orbital solution has an rms residual velocity comparable to the velocity measurement errors. As of 2019 July, we have over 9000 spectra spanning nearly 15 years for 1198 stars in the sample. The resulting RV measurements and first results from these data are presented in this paper.

4. RV Measurement and Precision

RVs for single narrow-lined stars (i.e., stars with $v \sin i < 10$ km s^{-1}) are derived from the centroid of a one-dimensional cross-correlation function (CCF) with an observed solar template at zero velocity, corrected for the individual fiber offsets of the Hydra MOS and converted to a heliocentric velocity. RVs for double-lined stars are derived following the two-dimensional cross-correlation technique TODCOR (Zucker & Mazeh 1994). Based on the analysis of Geller et al. (2008), we apply a quality threshold

requirement of CCF $\geqslant 0.4$ for our RV measurements. We present all of our RV measurements for each star in Table 1, along with the Heliocentric Julian Date (HJD) of the observation and the height of the cross-correlation function. We also include the RV residual and the orbital phase of the observation for binary stars with completed orbital solutions.

Following the procedure of Geller et al. (2008) and Tofflemire et al. (2014) of fitting a χ^2 distribution to our observed distribution of RV standard deviations, we find our precision, σ_i, for the NGC 7789 narrow-lined stars to be 0.3 ± 0.04 km s^{-1} (Figure 2). This value is consistent with the value of $\sigma_i = 0.4$ km s^{-1} used in previous WOCS papers, which we adopt here as a conservative estimate.

For stars in our sample that are rapidly rotating ($v \sin i > 10$ km s^{-1}), using an observed solar template results in a decrease in precision in our RV measurements due to their broadened CCFs. To achieve better RVs, we cross-correlate these stars against a grid of synthetic spectra[9] (Kurucz 1993; Meibom et al. 2009) with solar-metallicity, $\log g = 4.0$, $T_{eff} = 6500$ K (unless otherwise noted), and spanning a range

---

[9] The library is based on ATLAS9 (http://kurucz.harvard.edu) and the companion program SYNTHE used to compute the synthetic spectrum from the model atmosphere and line list.
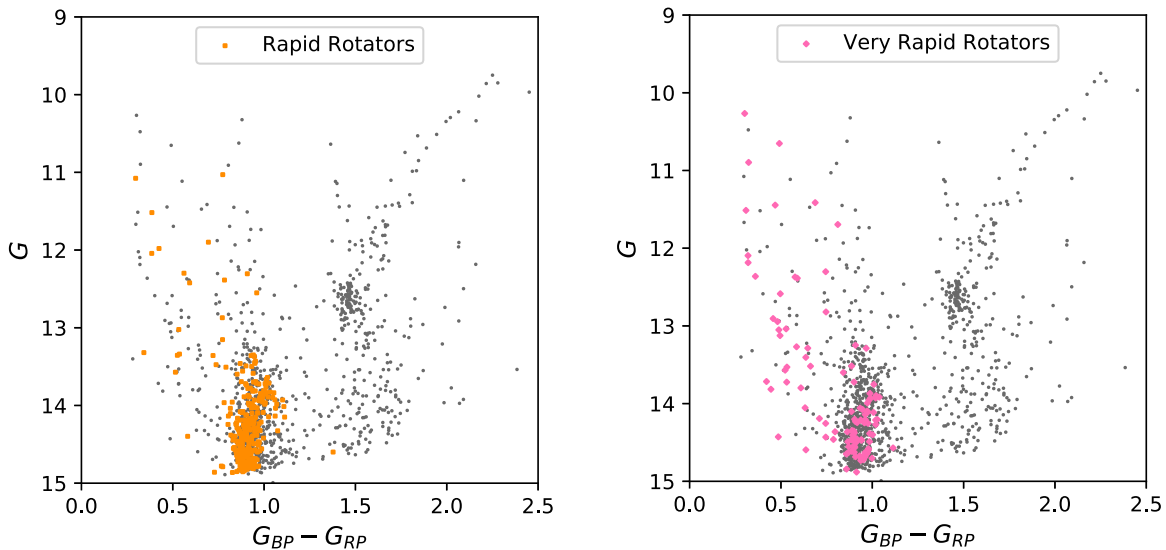
Figure 3. NGC 7789 CMD of the sample studied in this paper, constructed with Gaia DR2 photometry. Left panel: rapid rotators with $10\ \mathrm{km\ s^{-1}} < v \sin i < 120\ \mathrm{km\ s^{-1}}$ are shown by orange squares. Right panel: very rapid rotators with $v \sin i > 120\ \mathrm{km\ s^{-1}}$, for which we cannot derive accurate RVs, are shown with pink diamonds.

of projected rotation velocities. We selected these particular values for temperature and log g based on the parameters near the turnoff of a 1.6 Gyr isochrone generated by the MESA Isochrones & Stellar Tracks (MIST; Dotter 2016 and references therein), corresponding to the CMD position of the majority of the rapidly rotating stars (Figure 3). Adjusting the temperature of the synthetic spectra improved the RVs only for the hottest of stars in our sample. We note these stars and their best-matched temperatures (the highest cross-correlation peak height) in Table 2. For the stars with $v \sin i \geqslant 70\ \mathrm{km\ s^{-1}}$, we found an RV zero-point offset of $+1.8\ \mathrm{km\ s^{-1}}$ from the narrow-lined stars. Using the best-match template and applying this zero-point offset, we derive the RVs for RR stars presented in Table 1 and note the $v \sin i$ of the synthetic spectra in Table 2. We assign a precision to these rapid rotators (RRs) using the following relationship from Geller et al. (2010):

$$\sigma_i = 0.38 + 0.012(v \sin i). \tag{1}$$

The above procedure does not work consistently for stars with $v \sin i$ greater than $\sim 120\ \mathrm{km\ s^{-1}}$ because of their very broad CCFs. We label stars that are rotating faster than this as very rapid rotators (VRRs), and we are unable to get accurate RV measurements or RV membership information for these stars.

In our sample, we identified 273 RR and 113 VRR stars. We plot the CMD location of 270 of the RR stars and all 113 VRR stars in Figure 3. As expected, most of these stars are hot and blue, with $G_{\mathrm{BP}} - G_{\mathrm{RP}} \leqslant 1.0$, and are concentrated on the upper main sequence. These stars represent approximately 50% of the main-sequence stars in our sample.

5. Completeness

The target sample in this paper comprises 1206 stars with RV measurements starting in 2005. During our survey we constantly reevaluate the observing priority of each star. Generally we classify stars as single or velocity variable after three observations (Mathieu 1983; Geller & Mathieu 2012), and we then prioritize velocity-variable stars for continued observations until we determine an orbital solution. When we

identify a VRR we move it to the bottom of our observation priority because we are unable to derive accurate RVs for such RRs. The percentages of stars for which we have three or more observations (excluding VRRs) as a function of cluster radius and of G magnitude are shown in Figure 4. We are able to classify almost 99% of stars in our stellar sample of NGC 7789 as single (by which we mean non-velocity variable), velocity-variable, or as VRRs. There are no significant biases in the classified stars with radius or magnitude.

6. Results of the RV Study

6.1. Stellar RVs

For each star with three or more observations we calculate the mean $\overline{RV}$ and e/i, and classify it as single or velocity variable. We define velocity-variable stars as having RV standard deviations (the external error, e) greater than four times the precision (the internal error σ_i, or i, described in Section 4),[10] that is $e/i > 4$ (Geller et al. 2008). Based on a Monte Carlo analysis for the NGC 7789 RV measurements, this procedure identifies 84% of all binaries with periods under 1000 days and 60% of all binaries under 10,000 days (Section 8).

We present the coordinates, Gaia DR2 photometry, number of observations, $\overline{RV}$, $\overline{RV}$ standard error, e/i, proper-motion membership probability (P_μ; Section 6.3), RV membership probability (P_{RV}), and membership classification for all of the stars we have observed in NGC 7789 as of 2019 July in Table 2. For each binary star with a completed orbital solution, the center-of-mass velocity, γ, its error, and whether it is a single- or double-lined binary are also included in Table 2.

6.2. RV Membership Probabilities

We follow the standard WOCS procedure and calculate the RV membership probability of a given star, P_{RV}, in Table 2

---

[10] For consistency with previous WOCS papers and to prevent confusion with other uses of σ in this paper, we will use i to indicate internal precision for the rest of the paper.

Table 2
RV Summary Table

ID	α (J2000)	δ (J2000)	G	$G_{BP} - G_{RP}$	N	$\overline{RV}$ (km s^{-1})	Std. Err. (km s^{-1})	e/i	P_μ (%)	P_{RV} (%)	Class	γ_{RV} (km s^{-1})	γ_{RVe} (km s^{-1})	Comment
1001	23 57 24.11	56 43 38.8	13.93	0.95	19	−51.3	0.9	0.5	87	88	SM	⋯	⋯	RR (100 km s^{-1})
1002	23 57 18.72	56 43 50.8	13.73	0.94	3	−36.5	0.2	0.5	0	0	SNM	⋯	⋯	⋯
1003	23 57 29.55	56 42 23.5	12.33	1.47	3	−53.9	0.3	0.7	99	95	SM	⋯	⋯	⋯
1004	23 57 10.40	56 42 49.4	9.86	2.22	5	−53.6	0.2	0.5	99	95	SM	⋯	⋯	⋯
1005	23 57 31.85	56 41 22.1	11.1	1.69	3	−56.1	0.3	0.7	⋯	84	SM	⋯	⋯	⋯
1006	23 57 10.06	56 40 56.7	10.74	1.77	16	−53.1	2.1	5.2	89	93	BM	−54.96	0.18	SB1
1007	23 57 34.30	56 46 2.9	11.69	0.5	3	−4.0	0.1	0.3	0	0	SNM	⋯	⋯	⋯
1008	23 57 3.25	56 45 58.0	9.75	2.25	3	−53.5	0.1	0.2	99	95	SM	⋯	⋯	⋯
1009	23 57 52.04	56 42 25.6	10.29	2.02	3	−52.5	0.2	0.4	0	94	SNM	⋯	⋯	⋯
1010	23 57 43.94	56 39 42.8	11.51	0.31	11	18.9	3.8	9.5	0	⋯	VRR, NM	⋯	⋯	VRR

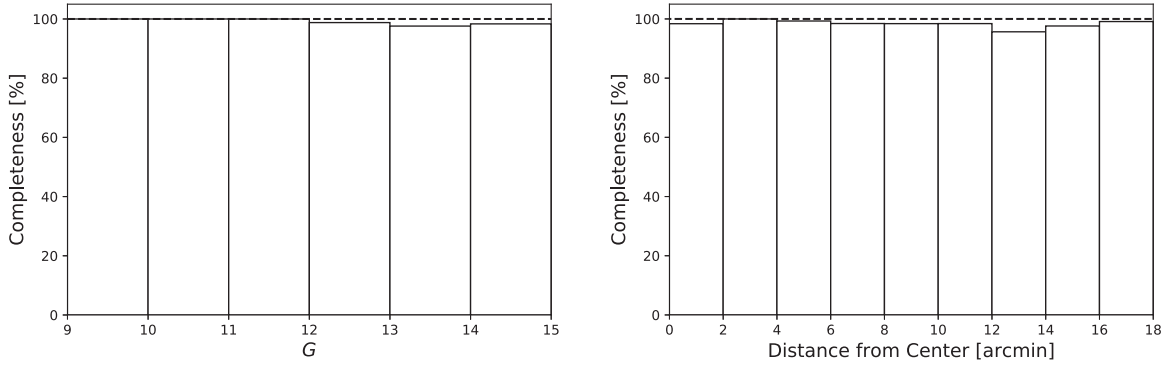(This table is available in its entirety in machine-readable form.)

Figure 4. Percentage of stars in our sample (excluding VRRs) that have three or more RV observations with respect to distance from the cluster center (left) and G magnitude (right).
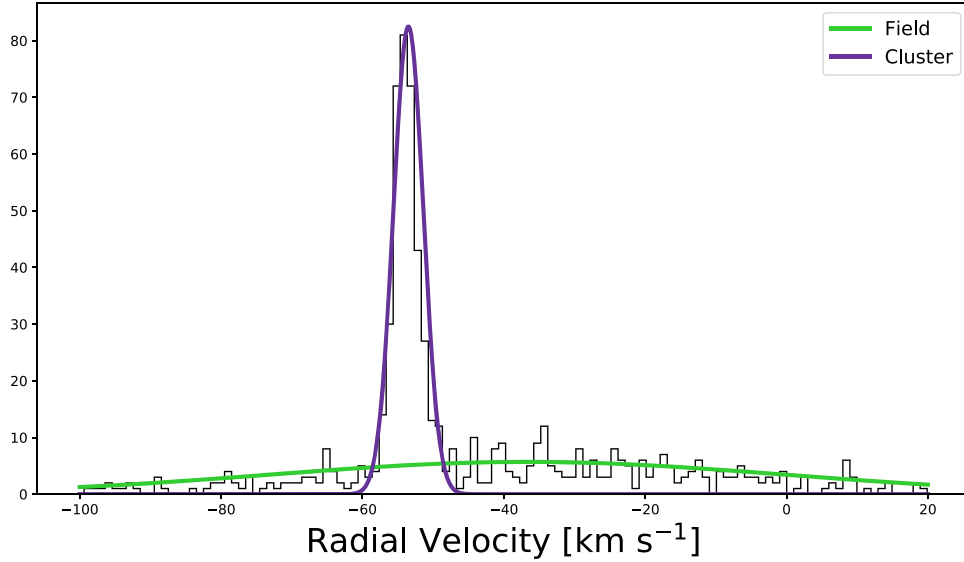

Figure 5. Histogram of the RV distribution of single stars, $e/i < 4$, with three or more RV observations. Also plotted are the Gaussian distributions fit to the cluster (the large peak at a mean velocity of -53.5 km s^{-1}; purple line) and the field (green line).

using the equation

$$P_{RV}(v) = \frac{F_{cluster}(v)}{F_{field}(v) + F_{cluster}(v)}. \qquad (2)$$

$F_{cluster}$ and F_{field} are Gaussian functions simultaneously fit to the cluster and field-star populations using our sample of all single stars with three or more RV measurements. We plot these RVs and Gaussian functions in Figure 5 and record the parameters for these Gaussian fits in Table 3.

The RV survey of giant stars by Gim et al. (1998a) found $\overline{RV} = -54.9 \pm 0.1$ km s^{-1} based on 50 stars, and the abundance study of Jacobson et al. (2011) found $\overline{RV} = -54.7 \pm 0.3$ km s^{-1} based on 26 evolved stars in NGC 7789. Overbeek et al. (2015) found $\overline{RV} = -54.6 \pm 0.2$ km s^{-1} based on their study of 32 evolved stars. We note that the uncertainties on the means cited here are computed by us based on the dispersions provided in these papers. Our Gaussian fit to the cluster distribution yields $\overline{RV} = -53.5 \pm 0.1$ km s^{-1}, a formally higher value than these studies. Our result is consistent with that of Casamiquela et al. (2016) who found a median RV of -53.6 ± 0.2 km s^{-1} for seven red clump stars in NGC 7789. Geller et al. (2008) and Geller et al. (2015) found that the WOCS RV system is on the same zero-point as the DAO (Fletcher et al. 1982) and Harvard–Smithsonian Center for Astrophysics (CfA; Latham et al. 1985) systems.

Table 3
Gaussian Fit Parameters for Cluster and Field RV Distributions

Parameter	Cluster	Field
Ampl. (number)	82.5 ± 3.3	5.7 ± 0.8
$\overline{RV}$ (km s^{-1})	-53.5 ± 0.1	-36.7 ± 4.5
σ (km s^{-1})	1.5 ± 0.1	25.7 ± 4.7

We note a clear separation between the cluster and field populations based on P_{RV} (Figure 6) and we adopt the standard WOCS membership threshold of $P_{RV} \geqslant 50\%$ for NGC 7789. We estimate from the cluster and field Gaussian functions a field-star contamination of 5% above this membership threshold.

6.3. Proper-motion Membership Probabilities

We compare our RV membership results to the astrometric data retrieved from Gaia DR2. We were able to obtain complete astrometric information for 1187 stars in our sample. For each of the sources returned, we check the associated astrometric excess noise (ϵ_i) and the significance of the excess noise (D), which determine the disagreement between the observations of a source and the best-fitting astrometric model. For our derivation of P_μ for this cluster, we reject those sources
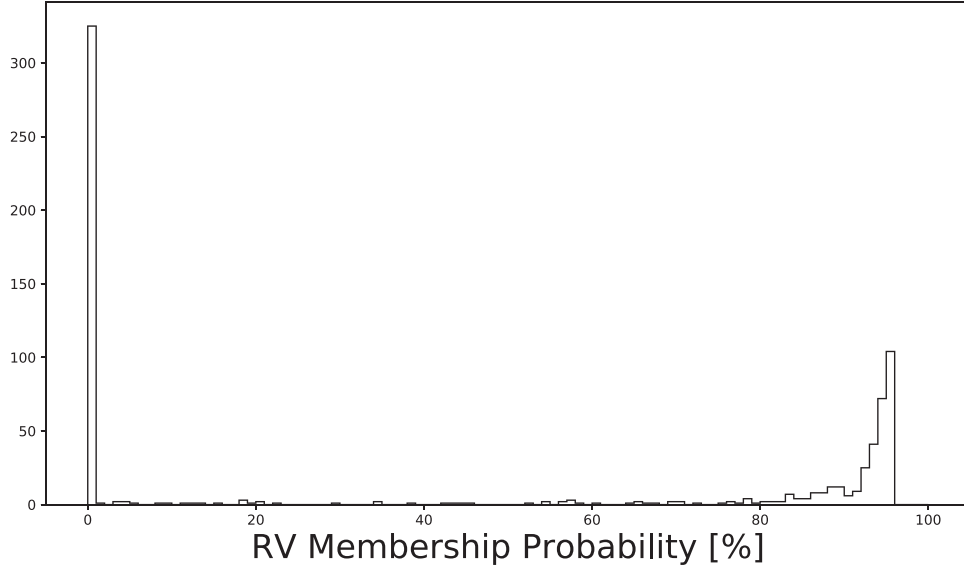
Figure 6. Histogram distribution of the RV membership probabilities of single stars (those with $e/i < 4$) in NGC 7789.
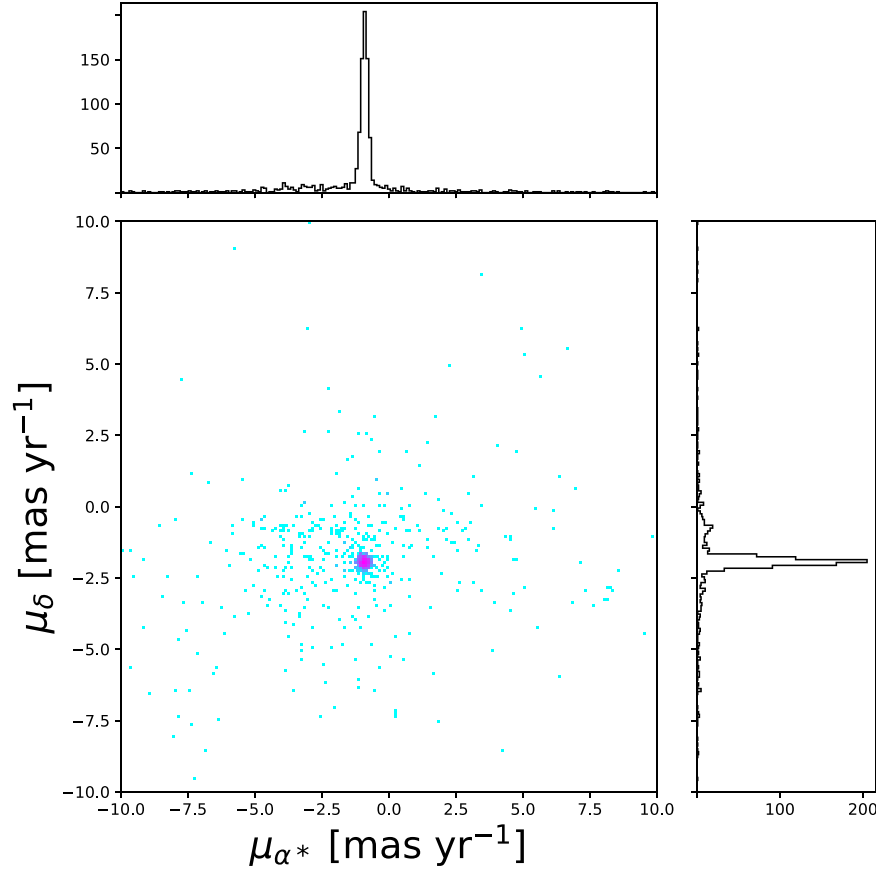

Figure 7. Two-dimensional histogram showing the Gaia DR2 proper motions of the stars in our sample in both R.A. and decl. On each axis we also plot the corresponding one-dimensional histogram in each direction. Cluster member stars appear as a clear overdensity in each plot, and in particular as a pink clump in the central plot.

which have $\epsilon_i \geqslant 10^{-3}$, which corresponds to $D \gtrsim 10^{-2}$. By rejecting these sources we aim to minimize the effects of any systematic variations in the astrometric data. We rejected a total of 85 stars from our sample, leaving 1102 stars with low-noise astrometry determined by Gaia DR2.

We use the astrometry from these 1102 stars to construct a two-dimensional Gaussian fit in proper-motion space in a similar manner as with the RVs. In this case, we fit two-dimensional Gaussian functions simultaneously to the proper motions of both cluster members and field stars. A more general description of this process is laid out in Gao (2018). We show the two-dimensional histogram of the proper motions obtained from Gaia DR2 in Figure 7, and the Gaussian fits are shown in Figure 8. We also show the parameters for these fits in Table 4.
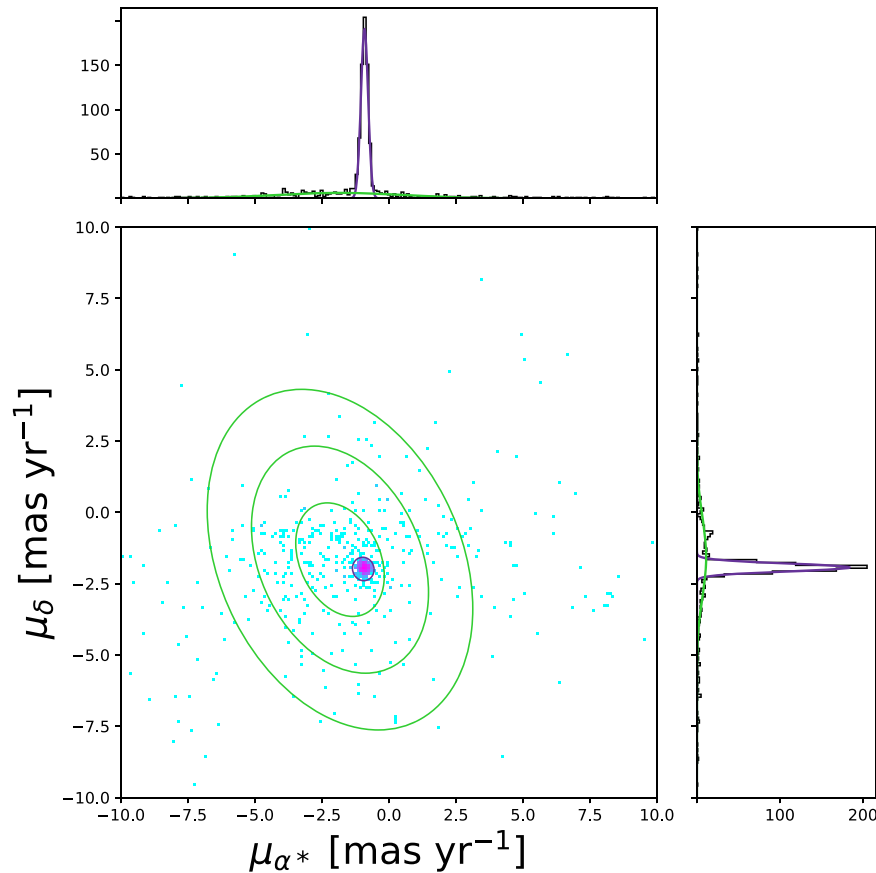
Figure 8. As in Figure 7, with the corresponding Gaussian fits overplotted. The fit to the cluster is tightly concentrated around the cluster proper motions in both the one-dimensional and two-dimensional cases, while the fit to the field is much more dispersed in proper-motion space. The contours in the central figure trace confidence intervals for both of the fits; the purple ellipse in the center traces the 6σ confidence interval for the cluster proper-motion distribution, while the green ellipses trace the 2, 4, and 6σ confidence intervals for the field distribution.

As with the RVs, there is a clear separation in P_μ between cluster and field populations, as shown in Figure 9. We again adopt the WOCS standard membership threshold of $P_\mu \geqslant 50\%$. We estimate from the amplitudes of the one-dimensional Gaussian functions fit to the cluster and field populations a field-star contamination of $\sim$4% above this threshold.

Where available we list the P_μ in Table 2. In Figure 10 we plot the membership percentages from our RV study and Gaia DR2 proper motions. We find the majority of stars that overlap between the data sets have membership classifications that agree. As noted above, we expect a field-star contamination of 5% within our sample of stars with $P_{RV} \geqslant 50\%$ based on the Gaussian fits to the cluster and field-star distribution. Comparing the P_μ and P_{RV} values we indeed find that $\sim$7% of the stars with $P_{RV} \geqslant 50\%$ have proper motions that identify them as field stars, as can be seen in Figure 10.

In Figure 10 there are 32 stars for which $P_{RV} < 50\%$ and $P_\mu > 50\%$. If these stars are all cluster nonmembers, they comprise $\sim$3% of our sample, also consistent with our estimate.

Finally, we note that out of our sample of three-dimensional kinematic members, there are 19 stars whose parallaxes are inconsistent with being cluster members based on a 5σ cut around the distribution of Gaia DR2 parallaxes for all three-dimensional cluster members. These stars are indicated in Table 2, and are removed from further discussion in this work.

Table 4
Two-dimensional Gaussian Fit Parameters for Cluster and Field Proper Motions

Parameter	Cluster	Field
Ampl. (number)	57.0 ± 1.3	0.2 ± 0.1
$\overline{\mu_{\alpha*}}$ (mas yr^{-1})	-0.959 ± 0.003	-1.8 ± 1.0
$\overline{\mu_\delta}$ (mas yr^{-1})	-1.986 ± 0.003	-1.6 ± 0.9
$\sigma_{\alpha*}$ (mas yr^{-1})	0.131 ± 0.003	1.5 ± 2.0
σ_δ (mas yr^{-1})	0.140 ± 0.004	1.9 ± 2.5

6.4. Membership Classification of Stars

Following previous WOCS procedure (Geller et al. 2015), we give in Table 2 membership classifications for stars in NGC 7789. The classifications are defined below for ease of reference here. Table 5 lists the number of stars in each membership classification.

Single Member (SM): stars that have $e/i < 4$, $P_{RV} \geqslant 50\%$, and $P_\mu \geqslant 50\%$.

Single Nonmember (SNM): stars that have $e/i < 4$ and either $P_{RV} < 50\%$ or $P_\mu < 50\%$.

Binary Member (BM): velocity-variable stars that have a completed orbital solution, $P_{RV} \geqslant 50\%$, and $P_\mu \geqslant 50\%$.

Binary Nonmember (BNM): velocity-variable stars that have a completed orbital solution and either $P_{RV} < 50\%$ or $P_\mu < 50\%$.
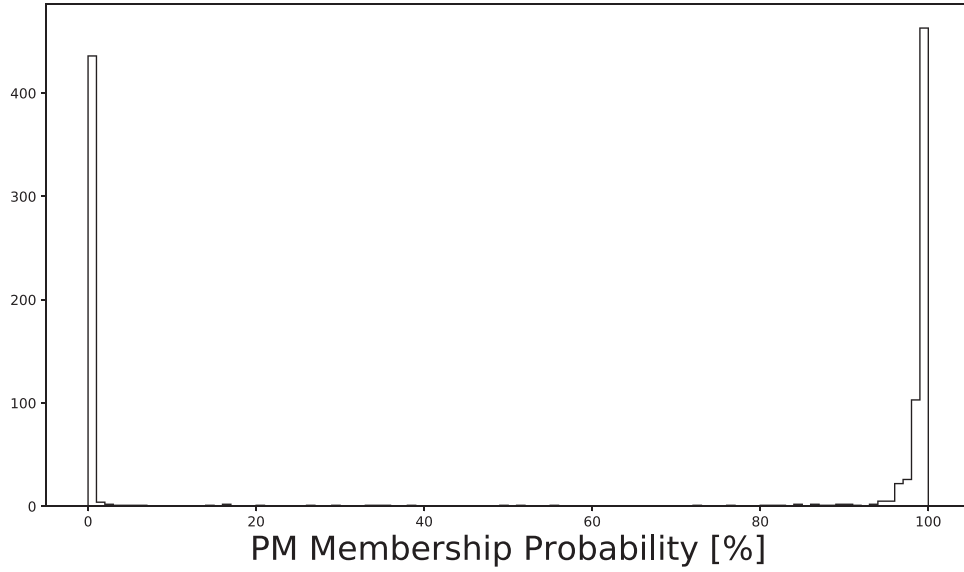
Figure 9. Histogram of the distribution of proper-motion membership probabilities for the stars with complete and low-noise astrometric data from Gaia DR2.
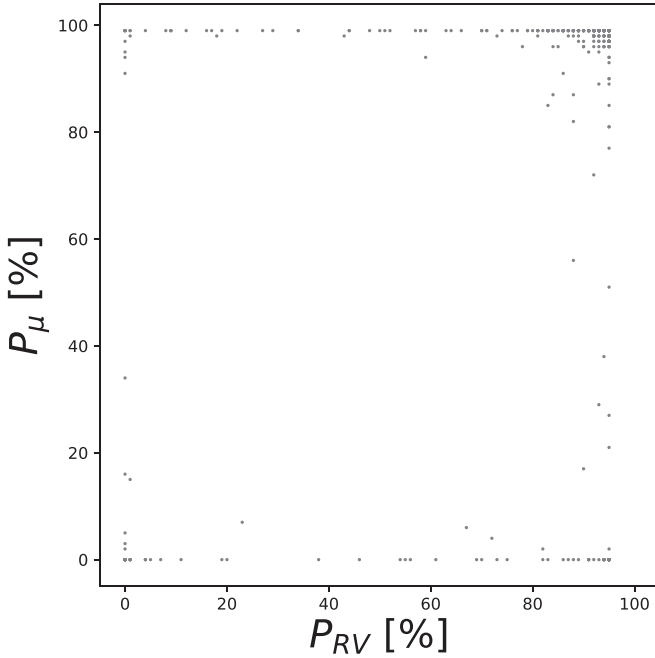

Figure 10. Comparison of RV membership probabilities with proper-motion membership probabilities ($n = 979$).

Table 5
Number of Stars within Each Classification

Classification	N Stars
SM	456
SNM	439
BM	81
BNM	32
BLM	21
BLN	33
BU	8
VRR, M	66
VRR, NM	45

Binary Likely Member (BLM): velocity-variable stars that do not have a completed orbital solution, $P_{RV} \geqslant 50\%$, and $P_\mu \geqslant 50\%$.

Binary Likely Nonmember (BLN): velocity-variable stars that do not have a completed orbital solution. Either P_{RV} or P_μ is $<50\%$ and the range of RVs does not include the cluster mean, making it unlikely that the orbital solution will place the star within the cluster distribution.

Binary Unknown (BU): velocity-variable stars that do not have a completed orbital solution. P_{RV} is $<50\%$, but P_μ is $\geqslant 50\%$, and the range of individual RVs includes the cluster mean, making it possible that the binary could be a member.

Very Rapid Rotator Likely Member (VRR, M): stars that are too rapidly rotating ($v \sin i > 120\,\mathrm{km\,s^{-1}}$) for accurate RV measurements, $P_\mu \geqslant 50\%$.

Very Rapid Rotator Likely Nonmember (VRR, NM): stars that are too rapidly rotating for accurate RV measurements, $P_\mu < 50\%$.

For those 85 stars discussed in Section 6.3 and the 6 discussed in Section 2 which do not have PM information available, we assign membership based solely on their RV information, using similar criteria as listed above.

6.5. Color–Magnitude Diagram

Using the Gaia DR2 photometry and our three-dimensional membership information, we present a cleaned CMD of NGC 7789 members in Figure 11. This CMD includes all three-dimensional BM, BLM, and SM stars. The cleaned CMD clearly shows the main sequence, crowded with velocity-variable stars, a very well-defined red giant branch (RGB), and a populous red clump at $G \sim 13$. A number of BSSs remain, which we discuss in more detail in Section 11.

We also show a 1.6 Gyr MIST (Dotter 2016) isochrone with a distance of 1.8 kpc, $A_V = 0.85$, and [Fe/H] = 0.023. These figures are roughly consistent with the heliocentric distance of $2075 \pm 4\,\mathrm{pc}$ as measured by Cantat-Gaudin et al. (2018), $E(B - V) = 0.28 \pm 0.02$ as measured by Wu et al. (2007), and [Fe/H] = 0.02 ± 0.04 as measured by Jacobson et al. (2011). The parameters used in our isochrone fitting are not meant to supersede those already published. Our isochrone is meant rather to guide the eye and serve as a reference point to distinguish between main-sequence stars and BSS candidates.
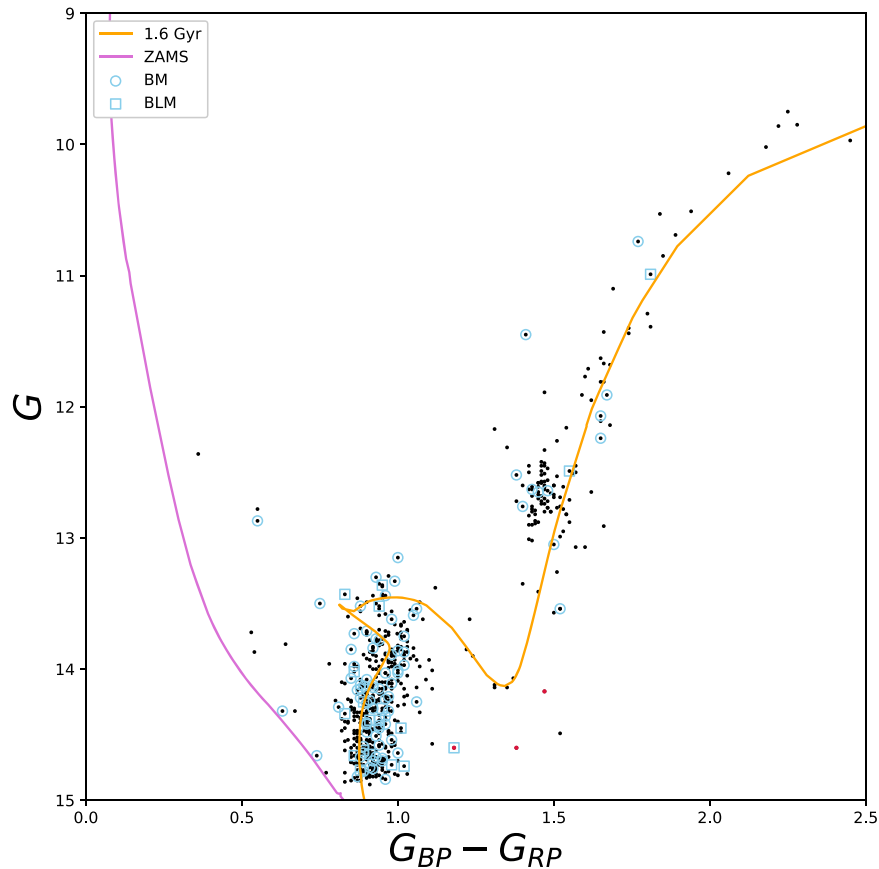
Figure 11. NGC 7789 CMD of all three-dimensional members (SM, BLM, and BM). We also include VRR, M stars. and a few members determined only by RV (Section 6.4) Velocity-variable stars are outlined in blue, using circles for BMs with completed orbital solutions and squares for BLMs without completed orbital solutions. We overplot a 1.6 Gyr MIST (Dotter 2016) isochrone in orange with a distance of 1.8 kpc, $A_V = 0.85$, and [Fe/H] = 0.023, as well as a ZAMS in lavender with the same parameters. The SSG and RSS candidates discussed in Section 6.6 are marked with red points.

6.6. Sub-subgiants and Red Stragglers

Two of the three-dimensional members are sub-subgiant (SSG) candidates that are fainter than the subgiant branch with $G_{BP} - G_{RP} \sim 1.2$–1.4. (Additional background on SSGs can be found in Geller et al. 2017a.) The candidates are WOCS 20035 and WOCS 35033. WOCS 20035 has $G_{BP} - G_{RP} = 1.18$, $P_{RV} = 95\%$, and $P_\mu = 99\%$. WOCS 35033 has $G_{BP} - G_{RP} = 1.38$, $P_{RV} = 94\%$, and $P_\mu = 93\%$. WOCS 20035 is velocity variable with a low amplitude of $\sim 7\,\mathrm{km\,s^{-1}}$, but does not yet have a complete orbital solution. WOCS 35033 is a rapid rotator with a best-fit $v \sin i$ of $120\,\mathrm{km\,s^{-1}}$; at the somewhat poorer measurement precision of $\sim 2\,\mathrm{km\,s^{-1}}$ we have not detected velocity variability. They are both targets of ongoing RV measurements. Neither of these candidates have been observed to be photometrically variable, as has been the case for other stars in these classes (Geller et al. 2017a). X-ray observations are not available.

We also note a three-dimensional member that lies to the red of the base of the RGB: WOCS 22023 ($G = 14.2$, $G_{BP} - G_{RP} = 1.47$, $P_{RV} = 94\%$, and $P_\mu = 99\%$). This region of the CMD is consistent with red straggler stars (RSS; more background also can be found in Geller et al. 2017a). Geller et al. (2017a) note that out of the seven RSS candidates they identify, four of them were found to be X-ray sources and three were found to be photometric or velocity variables. The three RV measurements of this RSS candidate acquired to date do

not meet our velocity-variability threshold, nor has it been observed to be either photometrically variable or an X-ray emitter by the X-ray Multi-Mirror Mission (XMM-Newton).

We have considered the effects of differential reddening across the cluster, which might preferentially redden some stars in our sample. We used dust maps produced by Bayestar (Green et al. 2019 and references therein), from which we obtained values for $E(B - V)$ for every star with a spatial resolution of $3'.4$. Using the transformation from Equation (1) of Gaia Collaboration et al. (2018a), we converted the obtained $E(B - V)$ values into the bandpasses of Gaia DR2. From this analysis we find that the dereddened and de-extincted color and magnitude of WOCS 20035 could be consistent with it being on the main sequence, acknowledging the limited spatial resolution of the reddening map. WOCS 35033 and WOCS 22023 remain SSG and RSS candidates, respectively.

WOCS 35033 is a particularly interesting case given its rapid rotation without an evident tidally locked close companion, which has been a common feature of the known SSG population. It may be akin to the recently discovered blue lurkers, hypothesized to have mass transfer or merger origins (Leiner et al. 2019). Neither evidently explains its current CMD location, although. Leiner et al. (2017) have suggested that large spots associated with rapid rotation of subgiants may be the cause of SSG CMD positions.
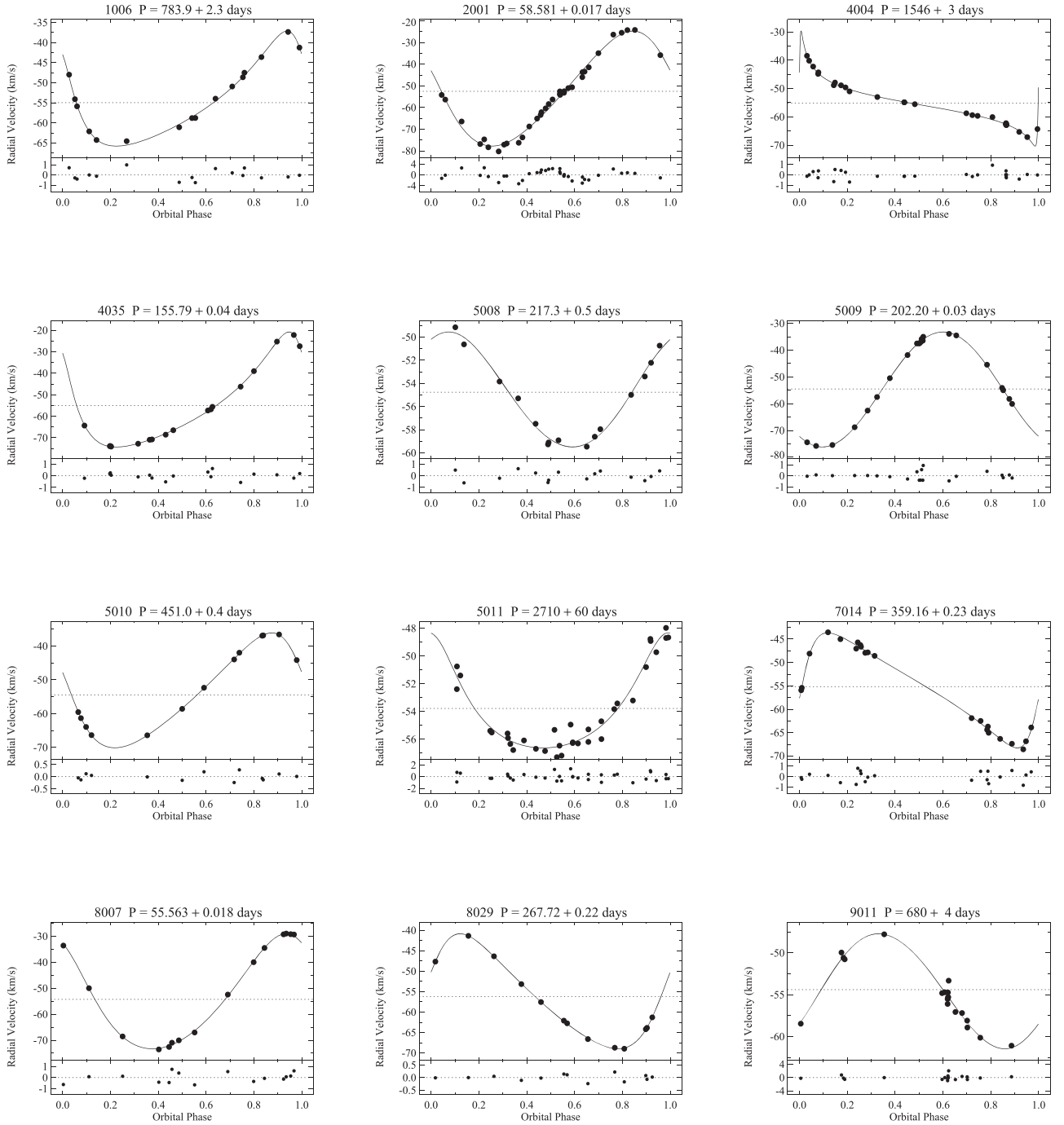
Figure 12. NGC 7789 orbit plots for each SB1, showing RV in the top panel and residuals from the fit in the lower panel, both as a function of orbital phase. Filled circles indicate the data points, the solid line is the orbital fit to the data, and the dotted line marks the γ velocity.

There are two other stars in the SSG region of the CMD: WOCS 35029 ($G = 14.49$, $G_{BP} - G_{RP} = 1.52$) and WOCS 36035 ($G = 14.57$, $G_{BP} - G_{RP} = 1.11$). WOCS 35029 has high-noise astrometry, and as such does not have a reliable P_μ. It is a non-velocity-variable RV member. WOCS 36035 is a VRR, M, and as such we do not have a reliable P_{RV}. When considering differential reddening, WOCS 36035 could be on the main sequence. WOCS 35029, however, remains in the SSG region of the CMD when taking differential reddening into account. Because of their potential scientific interest, both stars are shown on the CMD of Figure 11. We do not label them as RSS or SSGs at this time because we cannot say with the same level of certainty that they are cluster members.

7. Spectroscopic Binary Orbits

7.1. Single-lined Orbital Solutions

Using the data given in Table 1 we determine orbital solutions for 60 single-lined spectroscopic binaries (SB1). We show these orbit solutions in Figure 12. For each, the orbit solution is plotted in the top panel and the observed-minus-computed-residuals (O−C) are plotted in the bottom panel, both as a function of orbital phase. The orbital elements and their 1σ errors for each binary are listed in Table 6. The first row contains the binary ID, the orbital period (P), the number of orbital cycles observed, the center-of-mass RV (γ), the orbital amplitude (K), the eccentricity (e), the longitude of
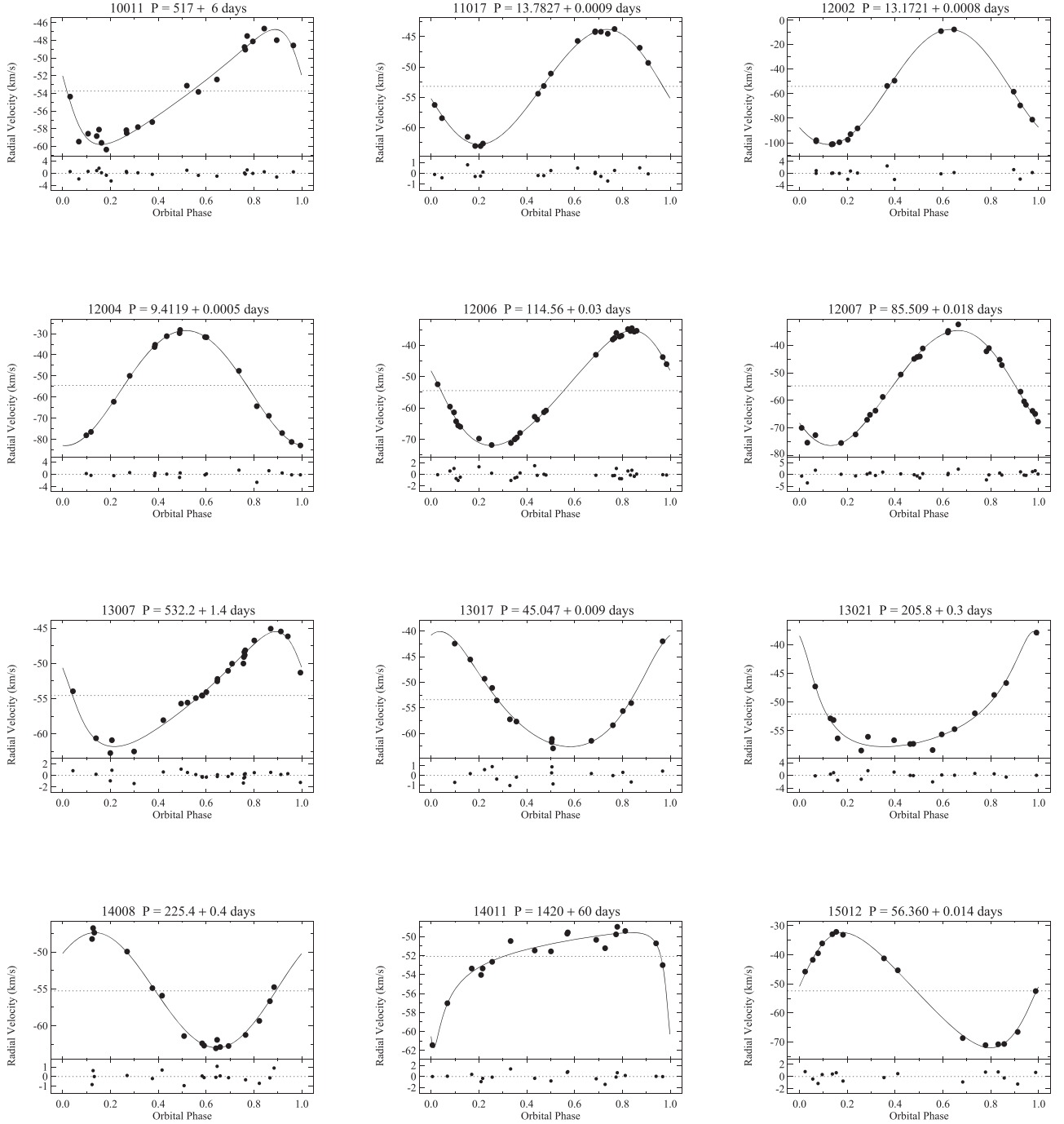
Figure 12. (Continued.)

periastron (ω), a Julian Date of periastron passage ($T_\circ$), the projected semimajor axis ($a \sin i$), the mass function ($f(m)$), the rms residual velocity from the orbital solution (σ), and the number of RV measurements (N). The second row contains the respective 1σ errors.

7.2. Double-lined Orbital Solutions

For double-lined spectroscopic binaries (SB2) we use TODCOR (Zucker & Mazeh 1994) which utilizes two template spectra to simultaneously derive RVs for the primary and secondary stars. For these binaries we used an observed solar spectrum for both templates.

We plot the SB2 orbital solutions in Figure 13. The top panel shows the primary RVs (filled circles) and fitted solution (solid line), the secondary RVs (open circles) and fitted solution (dashed line), as well as the γ velocity (dotted line). Square symbols ($\square$) represent data where the difference in velocities were below our spectral resolution of $20 \, \text{km s}^{-1}$, and were therefore not included in our orbital solutions. The bottom panel shows the O−C residuals for the primary (filled circles) and secondary (open circles).

Table 7 lists the orbital elements for each SB2. In the first row is the binary ID, the orbital period (P), the number of orbital cycles observed, the center-of-mass RV (γ), the orbital
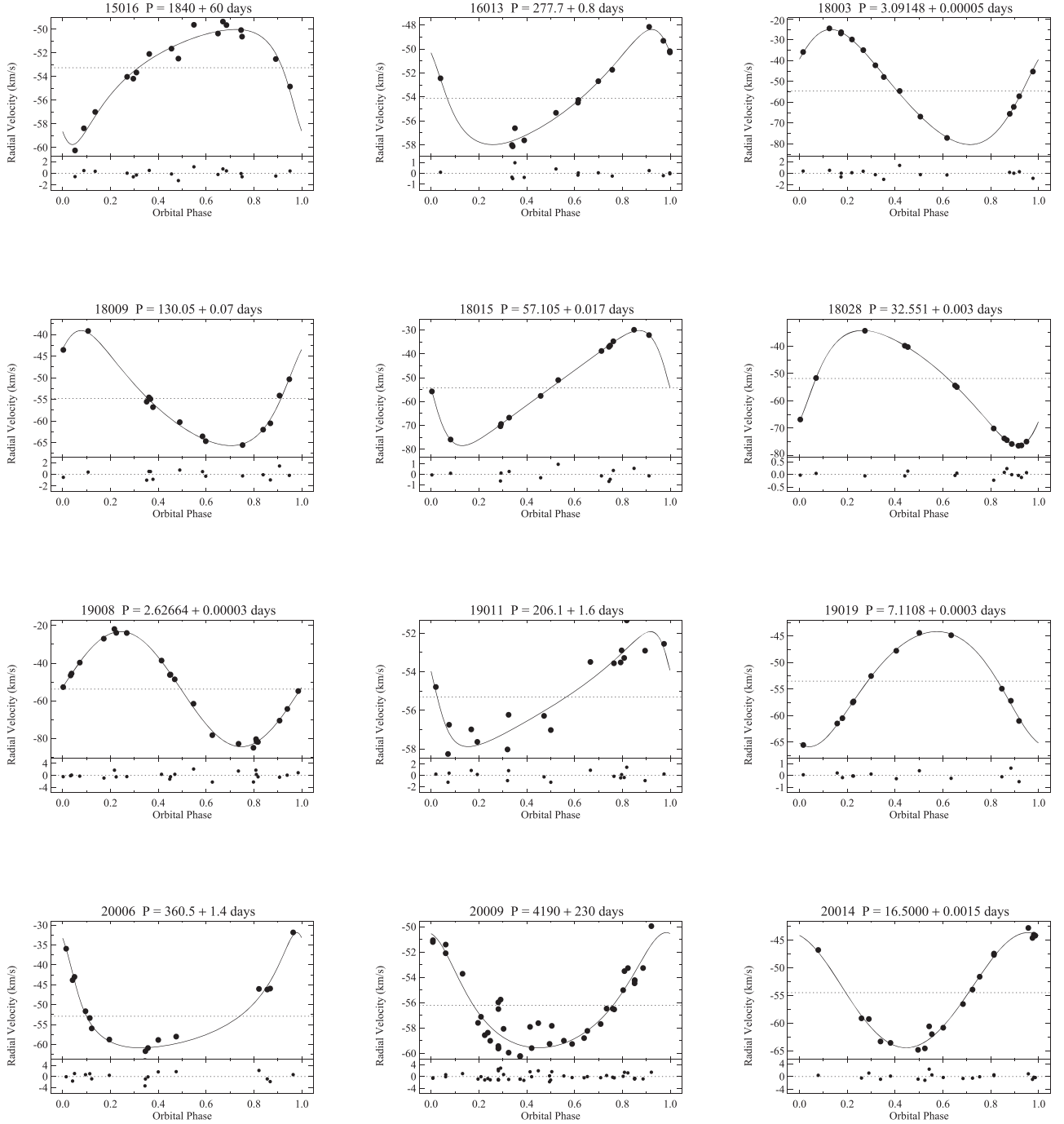
Figure 12. (Continued.)

amplitude of the primary (K), the eccentricity (e), the longitude of periastron (ω), a Julian Date of periastron passage ($T_\circ$), the projected primary semimajor axis ($a \sin i$), $m \sin^3 i$, the mass ratio (q), the rms residual velocity for the primary from the orbital solution (σ), and the number of RV measurements used in the orbital solutions after excluding measurements where the two velocities could not be resolved (N). The second row contains the respective 1σ errors on each of these values. The third and fourth rows are the amplitude (K), projected semimajor axis ($a \sin i$), $m \sin^3 i$, the rms residual velocity from the orbital solution (σ), and the number of resolved RV

measurements (N) for the secondary star and the respective errors.

8. Binary Frequency

8.1. Completeness in Binary Detection

We follow the Monte Carlo approach to our binary detection completeness described in Geller & Mathieu (2012). In brief, we generate observations of artificial binaries based on the Galactic field binary period and eccentricity distributions of Raghavan et al. (2010) and a random selection of mass ratio,
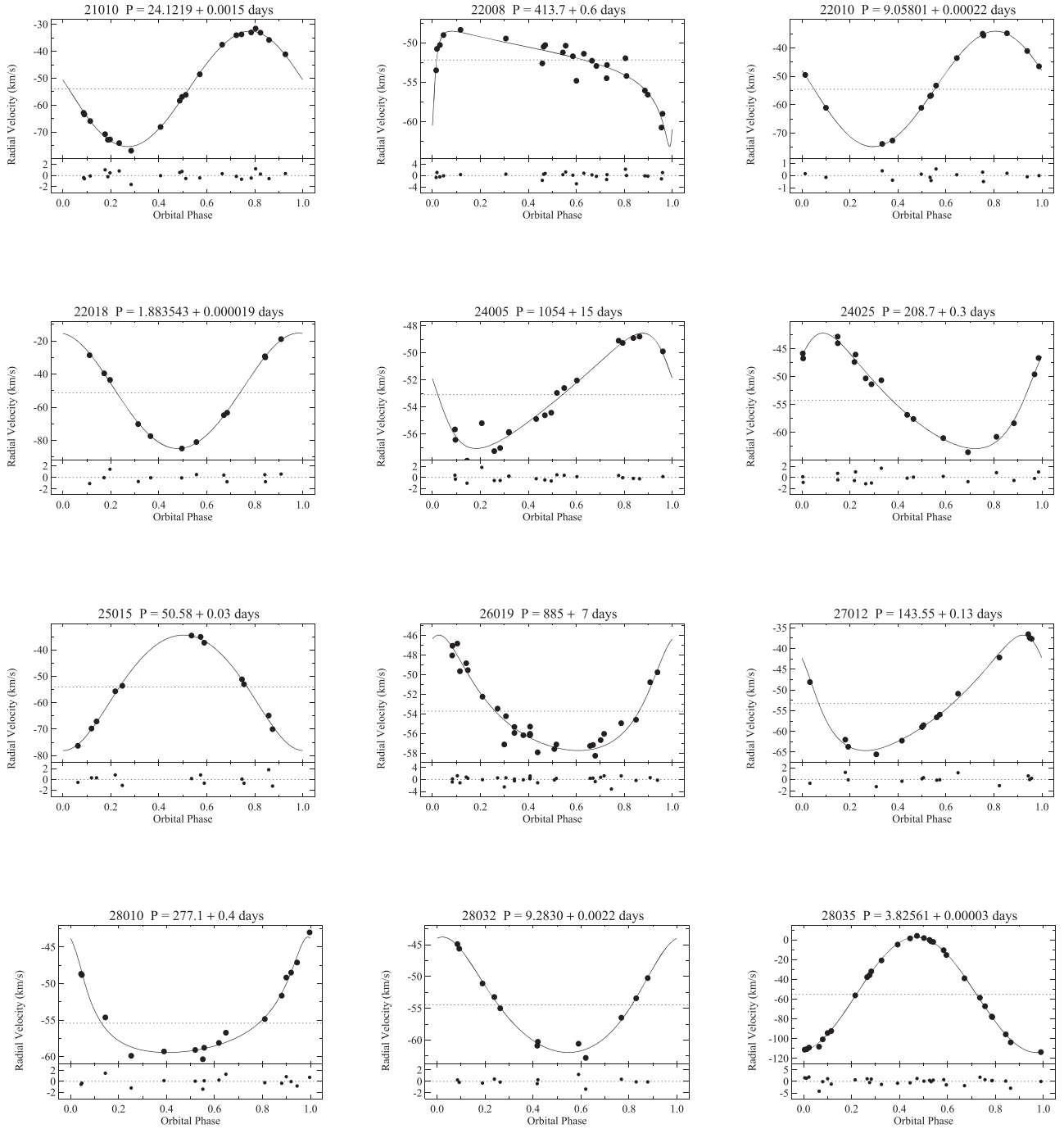
Figure 12. (Continued.)

orbital inclination, ω, and phase. We incorporate the measured tidal circularization period of NGC 7789 determined in Section 10. For each star we use the actual observation dates and precision value based on its $v \sin i$. From the detectability of these synthetic binaries we calculated a detection percentage of 84% for binaries with periods under 1000 days, 75% for periods under 3000 days, and 60% for periods under 10,000 days. These numbers are slightly less than the completeness percentages for NGC 188 (Geller & Mathieu 2012) and NGC 6819 (Milliman et al. 2014). This is due to the poorer precision associated with the rapidly rotating stars, which makes it more difficult to identify long-period, low-amplitude binary stars.

8.2. Main-sequence Binary Frequency

We find 230 single and 55 binary member and likely member stars on the main sequence of NGC 7789, restricting our analysis to $G \geqslant 14.0$ and $0.8 \leqslant G_{\rm BP} - G_{\rm RP} \leqslant 1.0$. We incorporate the 60% detection percentage to find a main-sequence binary frequency of $31\% \pm 4\%$ for binaries with periods less than 10^4 days.

The $P < 10^4$ days binary frequency found for other WOCS clusters include: $24\% \pm 3\%$ in M35 (150 Myr; Leiner et al. 2015), $22\% \pm 3\%$ in NGC 6819 (2.5 Gyr; Milliman et al. 2014), $34\% \pm 3\%$ in M67 (4 Gyr; A. M. Geller et al. 2020, in preparation), and
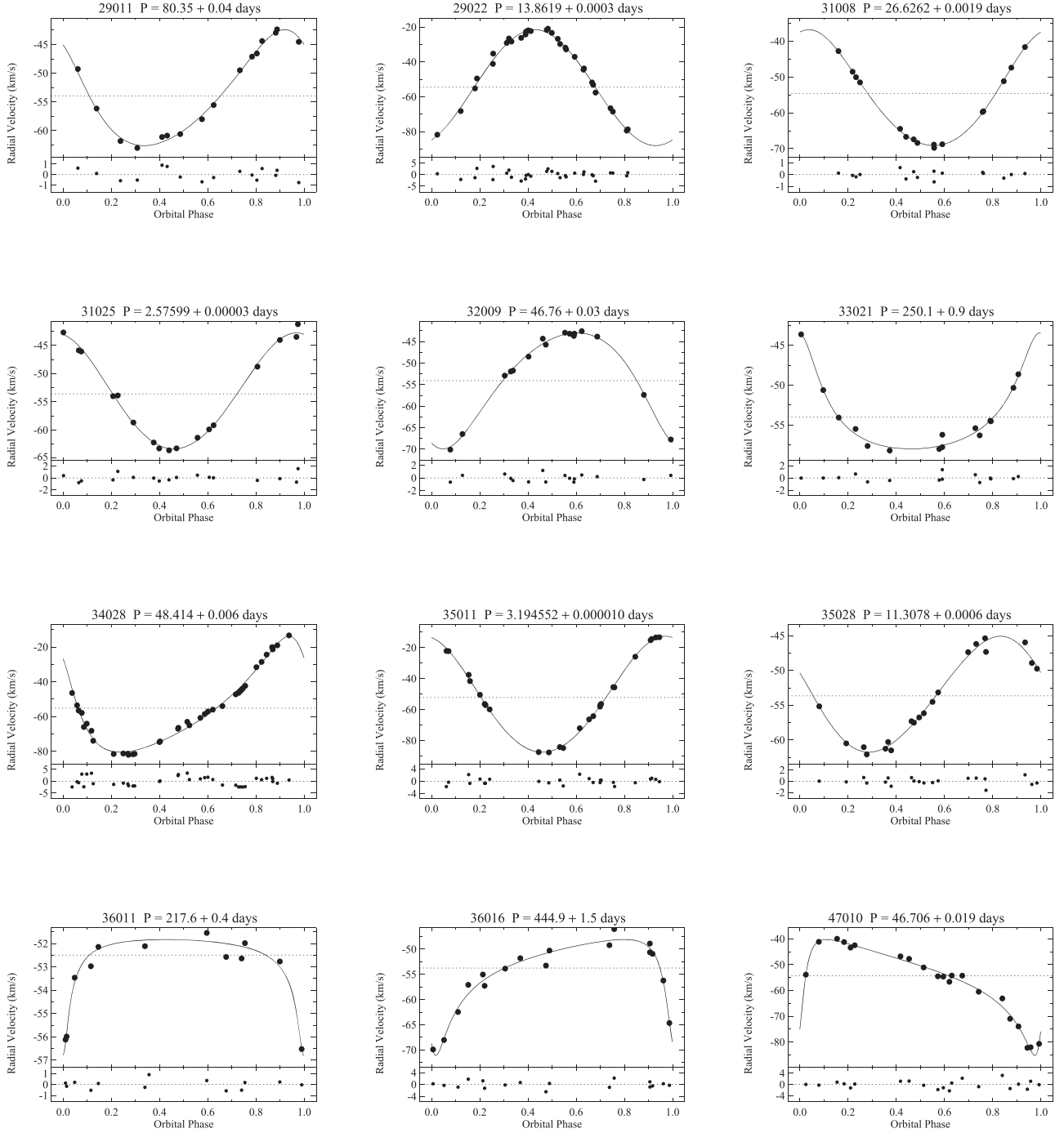
Figure 12. (Continued.)

29% ± 3% in NGC 188 (7 Gyr; Geller & Mathieu 2012). NGC 7789's value is consistent with these clusters.

The NGC 7789 main-sequence binary frequency is consistent with the binary frequency of 32% found by Gim et al. (1998b) in their RV study of giant stars in NGC 7789. This is perhaps surprising given that giant populations are deficient in close binary stars.

9. Photometric Variables

We have cross-referenced our stellar sample to the photometric variables found by Jahn et al. (1995), Mochejska & Kaluzny (1999), and Zhang et al. (2003), and list the results in Table 8.

Along with the photometric types and periods determined by these sources, we also list the orbital period for spectroscopic binaries, the $P_{\rm RV}$, P_μ, and any additional comments we have for the star.

Of the nine photometric variables that overlap with our NGC 7789 sample, we find three to be PM and RV members or likely members. WOCS 14014 and WOCS 17028, noted as eclipsing binaries by Mochejska & Kaluzny (1999) and Zhang et al. (2003), respectively, are SB2s with orbital solutions. The orbital period we find for WOCS 17028 is almost twice the eclipse period found by Mochejska & Kaluzny (1999). Zhang et al. (2003) do not fit a period to WOCS 14014 because of their short observing window and incomplete phase coverage.

Table 6
Orbital Parameters for NGC 7789 Single-lined Binaries

ID	P (days)	Orbital Cycles	γ (km s^{-1})	K (km s^{-1})	e	ω (deg)	$T_\circ$ (HJD-2,400,000 days)	$a \sin i$ (10^6 km)	$f(m)$ ($M_\odot$)	σ (km s^{-1})	N
1006	783.9	2.3	−54.96	14.3	0.413	54	55421	141	1.81e-1	0.63	16
	±2.3		±0.18	±0.3	±0.014	±3	±4	±3	±1.2e-2		
2001	58.581	55.7	−52.5	26.5	0.151	72	55049.4	21.1	1.10e-1	1.75	36
	±0.017		±0.4	±0.6	±0.022	±6	±1.0	±0.4	±0.7e-2		
4004	1546	1.3	−55.09	20	0.90	286	55144	190	1.2e-1	0.39	26
	±3		±0.19	±5	±0.05	±6	±4	±60	±1.0e-1		
4035	155.79	13.4	−55.02	26.77	0.442	50.8	54693.2	51.4	2.23e-1	0.35	17
	±0.04		±0.10	±0.15	±0.004	±0.8	±0.3	±0.3	±0.4e-2		
5008	217.3	9.4	−54.77	4.97	0.06	330	55042	14.8	2.8e-3	0.51	15
	±0.5		±0.14	±0.20	±0.05	±40	±22	±0.6	±0.3e-3		
5009	202.20	24.9	−54.50	21.48	0.011	140	54500	59.7	2.07e-1	0.39	21
	±0.03		±0.09	±0.14	±0.006	±40	±21	±0.4	±0.4e-2		
5010	451.0	4.9	−54.51	17.03	0.262	71.8	55146.4	101.9	2.07e-1	0.20	13
	±0.4		±0.07	±0.10	±0.005	±1.4	±1.6	±0.6	±0.4e-2		
5011	2710	1.4	−53.78	4.15	0.32	6	55980	147	1.71e-2	0.67	34
	±60		±0.13	±0.20	±0.04	±9	±60	±7	±2.5e-3		
7014	359.16	14.0	−55.15	12.30	0.484	262	55093.9	53.1	4.64e-2	0.54	22
	±0.23		±0.14	±0.19	±0.011	±3	±1.9	±0.9	±2.2e-3		
8007	55.563	37.7	−54.28	22.12	0.168	33	55027.5	16.66	5.97e-2	0.56	15
	±0.018		±0.23	±0.20	±0.011	±4	±0.6	±0.15	±1.6e-3		
8029	267.72	3.3	−56.17	14.07	0.269	289.4	56962.3	49.9	6.90e-2	0.17	13
	±0.22		±0.05	±0.08	±0.005	±1.3	±0.9	±0.3	±1.2e-3		
9011	680	3.5	−54.4	6.9	0.05	240	54950	64	2.3e-2	0.76	19
	±4		±0.3	±0.4	±0.05	±60	±120	±4	±0.4e-2		
10011	517	5.5	−53.7	6.5	0.37	79	56773	43	1.19e-2	1.14	22
	±6		±0.3	±0.4	±0.07	±10	±11	±3	±2.3e-3		
11017	13.7827	160.5	−53.21	9.50	0.053	102	55167.6	1.80	1.22e-3	0.46	17
	±0.0009		±0.13	±0.15	±0.024	±19	±0.8	±0.03	±0.6e-4		
12002	13.1721	217.2	−54.1	46.7	0.015	130	56546.5	8.46	1.39e-1	1.55	15
	±0.0008		±0.5	±0.6	±0.018	±60	±2.0	±0.12	±0.6e-2		
12004	9.4119	192.7	−54.5	27.2	0.044	175	54234.7	3.52	1.96e-2	1.06	17
	±0.0005		±0.3	±0.4	±0.015	±18	±0.5	±0.05	±0.8e-3		
12006	114.56	18.2	−54.49	18.34	0.151	73	54636.8	28.6	7.08e-2	0.74	29
	±0.03		±0.16	±0.21	±0.013	±5	±1.5	±0.3	±2.4e-3		
12007	85.509	58.8	−54.8	20.9	0.064	127	54961	24.6	8.1e-2	1.34	27
	±0.018		±0.3	±0.4	±0.019	±18	±4	±0.5	±0.5e-2		
13007	532.2	9.4	−54.57	8.2	0.30	68	54913	57.0	2.6e-2	0.74	26
	±1.4		±0.16	±0.3	±0.03	±5	±7	±1.9	±0.3e-2		
13017	45.047	104.3	−53.42	11.3	0.20	340	55229.3	6.84	6.3e-3	0.77	15
	±0.009		±0.22	±0.4	±0.03	±9	±1.1	±0.24	±0.6e-3		
13021	205.8	17.8	−52.1	10.0	0.47	22	55522	25.1	1.5e-2	1.13	16
	±0.3		±0.3	±0.6	±0.04	±11	±7	±1.7	±0.3e-2		
14008	225.4	9.6	−55.28	7.79	0.02	310	54590	24.1	1.10e-2	0.68	17
	±0.4		±0.19	±0.23	±0.04	±120	±80	±0.7	±1.0e-3		
14011	1420	1.8	−52.08	6.1	0.73	143	55459	81	1.0e-2	0.80	18
	±60		±0.20	±0.5	±0.03	±8	±15	±7	±0.3e-2		
15012	56.360	83.3	−52.4	19.8	0.188	274	55761.2	15.1	4.30e-2	0.90	15
	±0.014		±0.3	±0.3	±0.020	±6	±0.9	±0.3	±2.3e-3		
15016	1840	1.4	−53.25	4.9	0.43	141	54180	111	1.6e-2	0.71	17
	±60		±0.23	±0.5	±0.07	±8	±70	±11	±0.5e-2		
16013	277.7	9.3	−54.11	4.8	0.33	54	56935	17.3	2.7e-3	0.47	14
	±0.8		±0.21	±0.3	±0.06	±12	±6	±1.0	±0.4e-3		
18003	3.09148	925.2	−54.66	27.6	0.148	299	56395.40	1.162	6.6e-3	0.74	15
	±0.00005		±0.25	±0.5	±0.012	±5	±0.04	±0.020	±0.3e-3		
18009	130.05	19.9	−54.8	13.3	0.27	313	56733.9	22.9	2.8e-2	0.91	14
	±0.07		±0.3	±0.5	±0.03	±6	±2.1	±0.8	±0.3e-2		
18015	57.105	45.4	−54.33	24.1	0.386	90.2	56778.1	17.48	6.5e-2	0.63	13
	±0.017		±0.18	±0.3	±0.011	±2.3	±0.3	±0.24	±0.3e-2		
18028	32.551	22.7	−51.81	21.07	0.289	234.8	56913.66	9.03	2.77e-2	0.14	14
	±0.003		±0.06	±0.07	±0.003	±0.7	±0.05	±0.03	±0.3e-3		
19008	2.62664	576.0	−53.8	30.6	0.006	270	54877.9	1.107	7.8e-3	1.30	22
	±0.00003		±0.3	±0.4	±0.016	±110	±0.8	±0.016	±0.3e-3		
19011	206.1	8.9	−55.31	3.0	0.44	72	56277	7.6	4.1e-4	0.95	17

Table 6
(Continued)

ID	P (days)	Orbital Cycles	γ (km s^{-1})	K (km s^{-1})	e	ω (deg)	$T_\circ$ (HJD-2,400,000 days)	$a \sin i$ (10^6 km)	$f(m)$ ($M_\odot$)	σ (km s^{-1})	N
	±1.6		±0.24	±0.4	±0.10	±20	±8	±1.1	±1.7e-4		
19019	7.1108	159.9	−53.50	10.85	0.148	160	56087.61	1.049	9.1e-4	0.42	12
	±0.0003		±0.14	±0.22	±0.018	±8	±0.15	±0.022	±0.6e-4		
20006	360.5	5.5	−52.9	14.5	0.50	25	55066	62	7.3e-2	1.83	16
	±1.4		±0.5	±0.9	±0.04	±7	±4	±4	±1.4e-2		
20009	4190	0.9	−56.21	4.5	0.27	11	58390	253	3.6e-2	1.19	44
	±230		±0.21	±0.4	±0.09	±17	±160	±23	±1.0e-2		
20014	16.5000	304.8	−54.5	10.4	0.05	20	55194.7	2.36	1.92e-3	0.98	19
	±0.0015		±0.3	±0.3	±0.03	±50	±2.3	±0.07	±1.7e-4		
21010	24.1219	208.5	−54.04	21.46	0.017	80	55326	7.12	2.47e-2	0.78	21
	±0.0015		±0.19	±0.25	±0.013	±40	±3	±0.08	±0.9e-3		
22008	413.7	9.4	−52.2	7	0.79	231	55598	25	4.0e-3	1.19	24
	±0.6		±0.4	±4	±0.16	±17	±3	±17	±0.7e-2		
22010	9.05801	315.9	−54.58	20.33	0.019	72	56572.3	2.532	7.88e-3	0.39	14
	±0.00022		±0.13	±0.19	±0.010	±22	±0.5	±0.024	±2.2e-4		
22018	1.883543	691.1	−51.4	34.8	0.038	6	56442.86	0.900	8.2e-3	0.97	12
	±0.000019		±0.3	±0.5	±0.019	±17	±0.09	±0.013	±0.3e-3		
24005	1054	4.8	−53.09	4.3	0.32	78	54920	59	7.2e-3	0.72	19
	±15		±0.18	±0.3	±0.06	±13	±40	±4	±1.4e-3		
24025	208.7	10.6	−54.2	10.4	0.27	307	55136	28.7	2.2e-2	0.98	17
	±0.3		±0.3	±0.4	±0.04	±8	±4	±1.3	±0.3e-2		
25015	50.58	25.5	−54.1	21.9	0.10	179	56335	15.1	5.4e-2	1.22	12
	±0.03		±0.5	±0.6	±0.03	±20	±3	±0.4	±0.5e-2		
26019	885	3.8	−53.71	5.9	0.34	339	57460	67	1.5e-2	1.08	31
	±7		±0.23	±0.6	±0.09	±9	±19	±7	±0.5e-2		
27012	143.55	25.6	−53.3	13.9	0.31	53	55905.7	26.2	3.5e-2	0.91	14
	±0.13		±0.3	±0.4	±0.03	±6	±2.2	±0.8	±0.3e-2		
28010	277.1	14.9	−55.4	7.9	0.51	14	55402	26.0	9.1e-3	1.01	16
	±0.4		±0.3	±0.5	±0.04	±7	±3	±1.7	±1.7e-3		
28032	9.2830	113.5	−54.5	9.1	0.18	348	56465.5	1.14	6.9e-4	0.82	12
	±0.0022		±0.3	±0.8	±0.06	±18	±0.5	±0.10	±1.9e-4		
28035	3.825608	543.0	−55.2	58.4	0.006	190	54712.0	3.073	7.90e-2	1.54	29
	±0.000025		±0.3	±0.4	±0.007	±80	±0.9	±0.021	±1.6e-3		
29011	80.35	62.5	−53.93	10.1	0.19	42	55087.6	11.0	8.1e-3	0.67	16
	±0.04		±0.17	±0.3	±0.03	±8	±1.6	±0.3	±0.6e-3		
29022	13.8619	362.7	−54.5	33.3	0.007	210	54936	6.34	5.3e-2	1.72	31
	±0.0003		±0.4	±0.7	±0.017	±110	±4	±0.13	±0.3e-2		
31008	26.6262	82.7	−54.56	16.2	0.103	343	56334.2	5.90	1.15e-2	0.36	16
	±0.0019		±0.12	±0.3	±0.018	±6	±0.4	±0.13	±0.7e-3		
31025	2.57599	1823.0	−53.59	10.28	0.05	10	55158.94	0.364	2.89e-4	0.75	17
	±0.00003		±0.21	±0.23	±0.03	±30	±0.21	±0.008	±2.0e-5		
32009	46.76	88.5	−54.09	13.5	0.196	154	55585.5	8.49	1.11e-2	0.66	16
	±0.03		±0.21	±0.3	±0.023	±8	±1.2	±0.21	±0.8e-3		
33021	250.1	7.3	−54.02	7.3	0.46	6	55875	22.3	7.0e-3	0.66	15
	±0.9		±0.20	±0.5	±0.03	±9	±7	±1.4	±1.3e-3		
34028	48.414	97.0	−55.2	33.3	0.393	52	55374.1	20.4	1.44e-1	1.99	38
	±0.006		±0.4	±0.8	±0.018	±3	±0.3	±0.5	±1.1e-2		
35011	3.194552	1574.6	−52.2	37.5	0.058	13	55348.59	1.643	1.73e-2	1.12	25
	±0.000010		±0.3	±0.4	±0.008	±11	±0.10	±0.017	±0.5e-3		
35028	11.3078	415.2	−53.66	8.3	0.08	69	55289.3	1.29	6.7e-4	0.73	20
	±0.0006		±0.19	±0.3	±0.04	±22	±0.7	±0.04	±0.6e-4		
36011	217.6	17.9	−52.49	2.5	0.74	186	56029	5.0	1.1e-4	0.54	13
	±0.4		±0.17	±0.3	±0.09	±14	±6	±1.0	±0.5e-4		
36016	444.9	7.5	−53.7	11.5	0.64	142	55864	54	3.1e-2	1.39	17
	±1.5		±0.4	±0.7	±0.03	±5	±3	±4	±0.6e-2		
47010	46.706	103.6	−54.3	22.5	0.68	237	55374.74	10.6	2.2e-2	1.58	21
	±0.019		±0.4	±1.1	±0.03	±3	±0.21	±0.6	±0.4e-2		

(This table is available in machine-readable form.)

Another eclipsing binary, WOCS 11016, is an SB1 BSS candidate that has $P_\mu = 0\%$ and we consider it a field star. WOCS 13004 and WOCS 33005 are noted as W UMas. WOCS 13004 has a very high proper-motion membership probability, and we also classify it as a BU RR with $v \sin i = 110 \, \text{km s}^{-1}$. WOCS 33005 is a VRR, M with
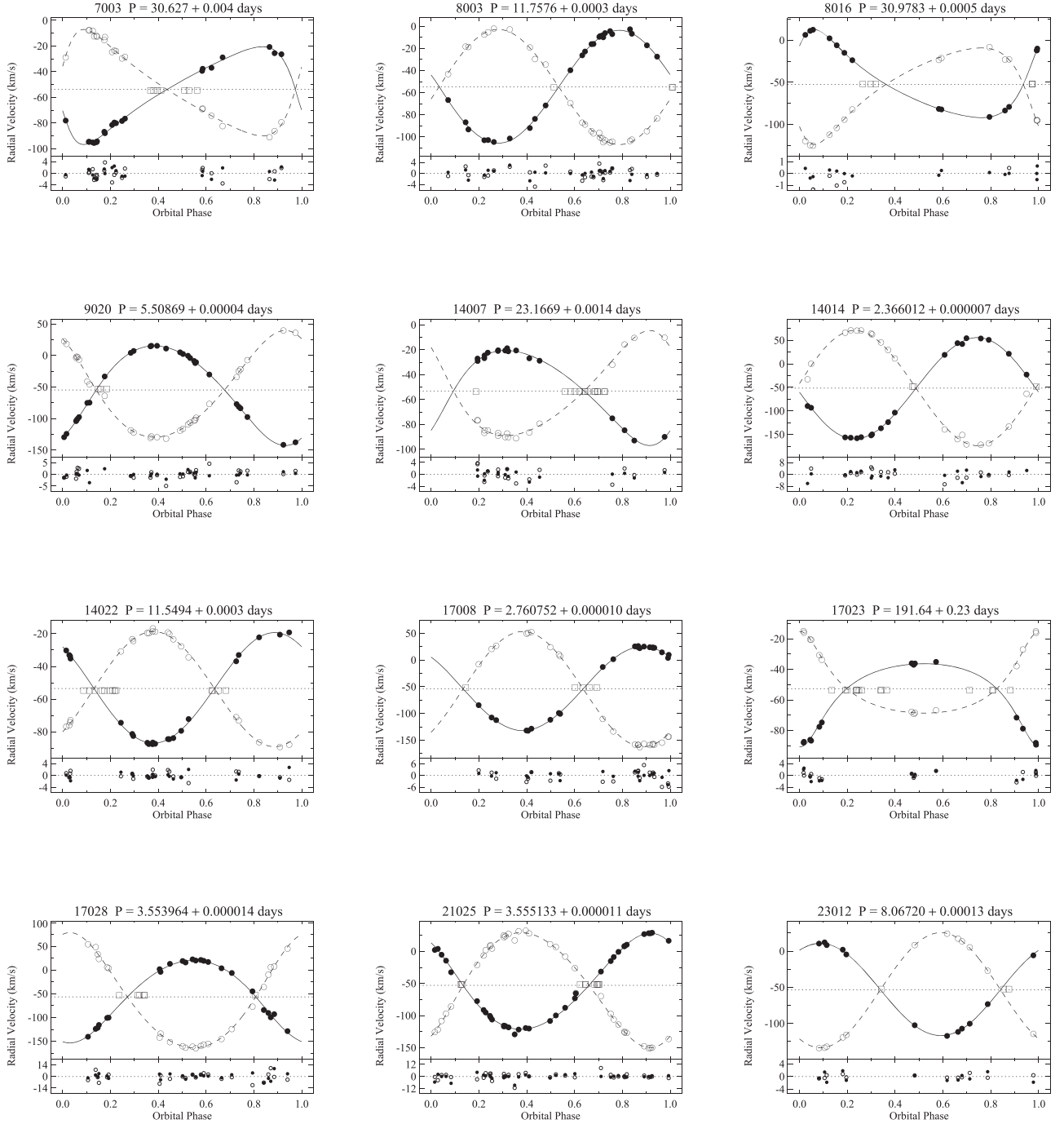
Figure 13. NGC 7789 SB2 orbit plots. We plot RV against orbital phase for each binary with the WOCS ID and orbital period above each plot. The data points and orbital fits for the primary star are represented by filled circles and a solid line. For the secondary star open circles and a dashed line represent the data points and the orbital fit, respectively. We mark the γ velocity with a dotted line. We show the residuals from the fit below each binary plot, using the same symbols.

$P_\mu = 97\%$. WOCS 20007 is detected by Jahn et al. ([1995](#)), but they did not have the time baseline to determine specifics about this system. We find it to be a binary which we classify as a BU. The one pulsating variable in this sample is a δ Scuti, WOCS 25008, which we find to be a single member of NGC 7789.

10. Tidal Circularization

In Figure [14](#) we plot the period–eccentricity distribution of NGC 7789, including only the main-sequence binary members

from 1 mag below the cluster turnoff ($G = 14$) to our magnitude limit of $G \sim 15$. This e-log P diagram is typical for open clusters, with a transition from small to zero eccentricities at short periods and a wide range of eccentricities at long periods. This distribution is the result of tidal processes acting over time to circularize the shorter period orbits. A notable binary is WOCS 21010, with a circular orbit at a period of 24 days, much longer than tidal circularization periods of any cluster.

We update the standard WOCS method to measure the tidal circularization period (CP) for NGC 7789. Following Meibom
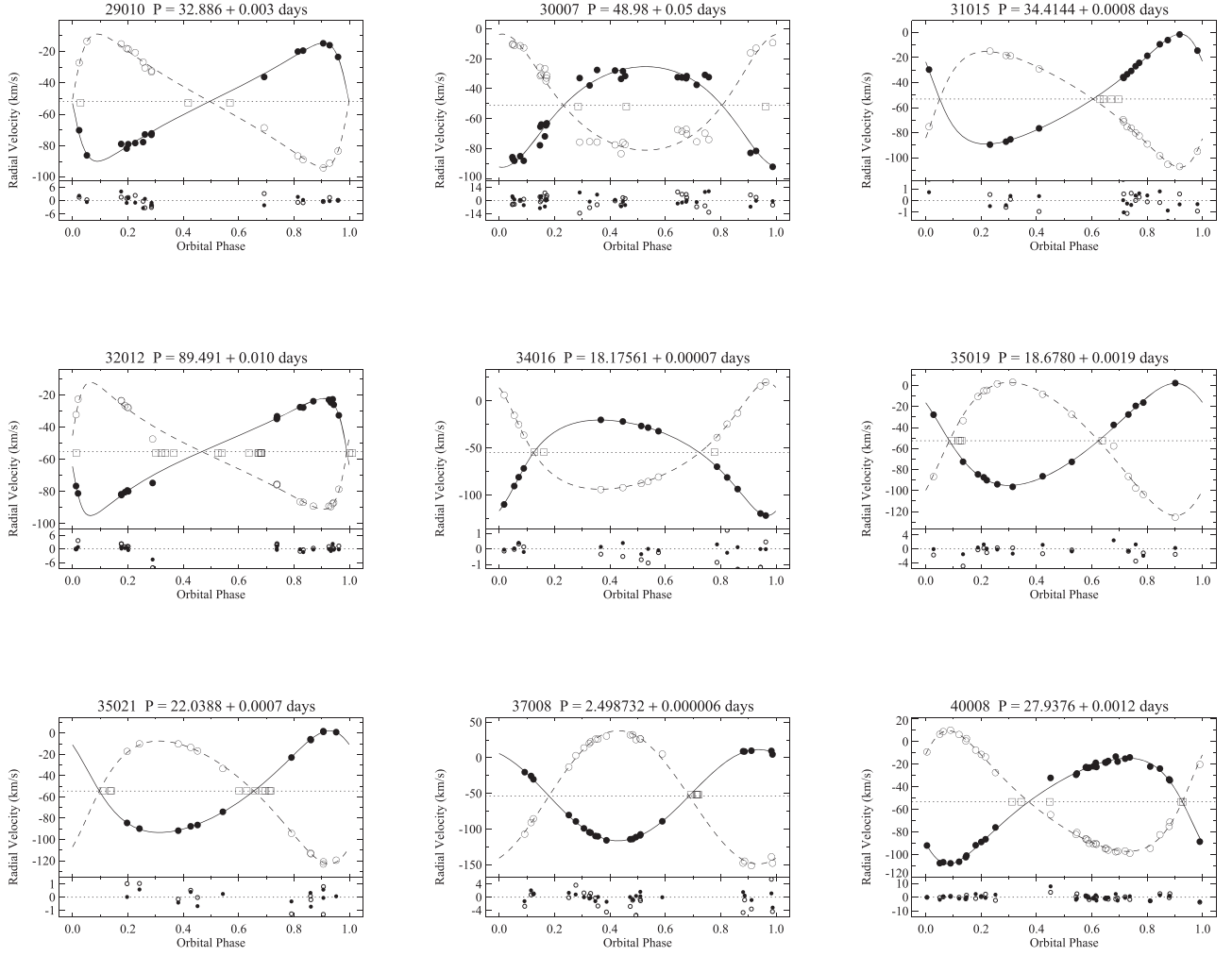
Figure 13. (Continued.)

& Mathieu (2005), we fit the piecewise function

$$e(P) = \begin{cases} 0.0 & \text{if } P \leqslant P', \\ \alpha \left(1 - e^{\beta(P'-P)}\right)^{\Gamma} & \text{if } P > P' \end{cases} \quad (3)$$

to the period–eccentricity distribution. Γ is set to 1.0, β is set to 0.14, and α is set to 0.35, the average eccentricity for binary orbits over 50 days in the Pleiades, M35, Hyades, M67, and NGC 188. Following A. M. Geller et al. (2020, in preparation), we use an orthogonal distance regression method to fit the circularization function, which accounts for the uncertainties on both the period and eccentricity. The CP is taken as the period at which the best-fit circularization function equals 0.01, or e (CP) = 0.01. Finally, we use a bootstrap technique to determine the cluster CP and its uncertainties.

We find the CP of NGC 7789 to be $7.2^{+0.6}_{-1.1}$ days, where the uncertainties are the 1σ percentile width of the trials around the median of the bootstrap trials distribution. Figure 15 shows the distribution of 50,000 trials. The distribution shows two peaks. We have selected the peak having the greatest weight in numbers of trials. However, with the current binary sample we cannot rule out a CP ~ 14 days.

Meibom & Mathieu (2005) measured CPs for eight solar-like binary populations: pre-main-sequence (PMS), Pleiades, M35,

Hyades and Praesepe, M67, NGC 188, the field, and the galactic halo to investigate tidal evolution rates, and thereby mechanisms, in solar-like stars. Since then the CP of the open cluster NGC 6819 was measured by Milliman et al. (2014), Leiner et al. (2015) updated the value for M35, and A. M. Geller et al. (2020, in preparation) updated the value for M67. With this work we add the CP of NGC 7789 and plot the most current CP measurements versus population age in Figure 16. (Only the NGC 7789 and M67 CPs are derived with the new bootstrap algorithm. This approach finds values for CP consistent with prior work, but having different uncertainties.)

We also include the predictions of three models of tidal circularization: significant circularization happening only during the PMS phase (Zahn & Bouchet 1989), the representation of main-sequence tidal circularization theory from the binary-star evolution (BSE) code of Hurley et al. (2002), and an ad hoc empirical model from Geller et al. (2013) that combines the PMS circularization from Kroupa (1995) and the BSE main-sequence circularization from Hurley et al. (2002) but with an artificially increased convective damping term tuned to match the distribution of tidal circularization period with cluster age. As noted in previous papers, neither of the theoretical models reproduce the observed dependence of tidal circularization with time for solar-like stars.

Table 7
Orbital Parameters for NGC 7789 Double-lined Binaries

ID	P (days)	Orbital Cycles	γ (km s^{-1})	K (km s^{-1})	e	ω (deg)	$T_\circ$ (HJD-2,400,000 days)	$a \sin i$ (10^6 km)	$m \sin^3 i$ ($M_\odot$)	q	σ (km s^{-1})	N
7003	30.627	66.5	−53.8	38.1	0.415	108	55064.24	14.59	0.626	0.919	1.68	21
	±0.005	⋯	±0.3	±0.6	±0.012	±2	±0.14	±0.24	±0.025	±0.020	⋯	⋯
	⋯	⋯	⋯	41.4	⋯	⋯	⋯	15.9	0.575	⋯	1.91	21
	⋯	⋯	⋯	±0.7	⋯	⋯	⋯	±0.3	±0.022	⋯	⋯	⋯
8003	11.7576	399.2	−54.78	51.1	0.011	80	55045	8.26	0.677	0.981	1.43	26
	±0.0003	⋯	±0.24	±0.4	±0.006	±40	±1	±0.07	±0.016	±0.013	⋯	⋯
	⋯	⋯	⋯	52.1	⋯	⋯	⋯	8.43	0.663	⋯	1.99	26
	⋯	⋯	⋯	±0.5	⋯	⋯	⋯	±0.09	±0.013	⋯	⋯	⋯
8016	30.9783	151.6	−52.4	52.3	0.393	308.7	55313.130	20.52	1.73	0.913	0.34	15
	±0.0005	⋯	±0.1	±0.1	±0.002	±0.5	±0.025	±0.07	±0.06	±0.015	⋯	⋯
	⋯	⋯	⋯	57.4	⋯	⋯	⋯	22.5	1.58	⋯	2.55	15
	⋯	⋯	⋯	±0.8	⋯	⋯	⋯	±0.4	±0.03	⋯	⋯	⋯
9020	5.50869	852.8	−54.59	79.1	0.137	213	54878.02	5.94	1.26	0.936	1.23	29
	±0.00005	⋯	±0.24	±0.4	±0.004	±2	±0.03	±0.03	±0.04	±0.014	⋯	⋯
	⋯	⋯	⋯	84	⋯	⋯	⋯	6.34	1.175	⋯	3.96	29
	⋯	⋯	⋯	±1	⋯	⋯	⋯	±0.09	±0.022	⋯	⋯	⋯
14007	23.167	217.2	−53.0	38	0.219	227	54571.61	11.9	0.61	0.905	1.25	17
	±0.001	⋯	±0.3	±1	±0.022	±4	±0.23	±0.3	±0.05	±0.023	⋯	⋯
	⋯	⋯	⋯	42	⋯	⋯	⋯	13.1	0.55	⋯	2.33	17
	⋯	⋯	⋯	±1	⋯	⋯	⋯	±0.4	±0.04	⋯	⋯	⋯
14014	2.36601	1748.0	−51.6	107.5	0.020	94	55371.60	3.50	1.58	0.880	2.87	19
	±0.00001	⋯	±0.7	±0.9	±0.009	±26	±0.17	±0.03	±0.07	±0.019	⋯	⋯
	⋯	⋯	⋯	122.2	⋯	⋯	⋯	3.97	1.39	⋯	7.68	19
	⋯	⋯	⋯	±2.2	⋯	⋯	⋯	±0.08	±0.04	⋯	⋯	⋯
14022	11.5494	180.1	−53.5	33.9	0.015	40	54550	5.38	0.201	0.960	1.13	22
	±0.0003	⋯	±0.2	±0.3	±0.009	±30	±1	±0.06	±0.005	±0.014	⋯	⋯
	⋯	⋯	⋯	35.2	⋯	⋯	⋯	5.60	0.193	⋯	1.23	22
	⋯	⋯	⋯	±0.4	⋯	⋯	⋯	±0.06	±0.005	⋯	⋯	⋯
17008	2.76075	1701.8	−53.8	78.6	0.007	40	55011.4	2.984	1.070	0.730	1.85	23
	±0.00001	⋯	±0.4	±0.5	±0.006	±50	±0.4	±0.021	±0.021	±0.008	⋯	⋯
	⋯	⋯	⋯	107.7	⋯	⋯	⋯	4.09	0.781	⋯	3.13	23
	⋯	⋯	⋯	±0.8	⋯	⋯	⋯	±0.04	±0.013	⋯	⋯	⋯
17023	191.64	8.6	−52.6	27.1	0.401	176	57035	65.5	1.18	1.02	1.73	14
	±0.23	⋯	±0.3	±0.5	±0.012	±6	±2	±1.7	±0.06	±0.03	⋯	⋯
	⋯	⋯	⋯	26.7	⋯	⋯	⋯	64.4	1.20	⋯	1.18	14
	⋯	⋯	⋯	±0.4	⋯	⋯	⋯	±1.2	±0.07	⋯	⋯	⋯
17028	3.553964	1415.9	−56.5	86.9	0.119	166	54711.71	4.22	1.89	0.717	3.86	24
	±0.000014	⋯	±0.6	±1.5	±0.014	±5	±0.04	±0.07	±0.08	±0.014	⋯	⋯
	⋯	⋯	⋯	121.2	⋯	⋯	⋯	5.88	1.39	⋯	5.28	24
	⋯	⋯	⋯	±2.0	⋯	⋯	⋯	±0.10	±0.06	⋯	⋯	⋯
21025	3.555133	1227.0	−52.8	74.9	0.106	37	56430.56	3.64	0.880	0.84	2.53	35
	±0.000011	⋯	±0.3	±0.6	±0.006	±3	±0.03	±0.03	±0.017	±0.01	⋯	⋯
	⋯	⋯	⋯	89.7	⋯	⋯	⋯	4.36	0.735	⋯	3.18	35
	⋯	⋯	⋯	±0.7	⋯	⋯	⋯	±0.04	±0.013	⋯	⋯	⋯
23012	8.06720	354.4	−53.39	63.89	0.009	330	56378.9	7.09	1.367	0.803	1.50	12
	±0.00013	⋯	±0.21	±0.52	±0.004	±20	±0.4	±0.07	±0.016	±0.008	⋯	⋯
	⋯	⋯	⋯	79.53	⋯	⋯	⋯	8.82	1.099	⋯	0.64	12
	⋯	⋯	⋯	±0.24	⋯	⋯	⋯	±0.03	±0.021	⋯	⋯	⋯
29010	32.886	56.8	−51.9	37.6	0.522	91	56904.30	14.50	0.57	0.888	1.98	16
	±0.004	⋯	±0.4	±0.9	±0.012	±2	±0.14	±0.34	±0.03	±0.025	⋯	⋯
	⋯	⋯	⋯	42.34	⋯	⋯	⋯	16.3	0.51	⋯	2.04	16
	⋯	⋯	⋯	±0.98	⋯	⋯	⋯	±0.4	±0.03	⋯	⋯	⋯
30007	48.98	53.6	−51.2	33.6	0.23	173	57123	22.0	0.952	0.87	4.91	29
	±0.05	⋯	±0.7	±1.6	±0.04	±9	±1	±1.0	±0.114	±0.05	⋯	⋯
	⋯	⋯	⋯	38.8	⋯	⋯	⋯	25.4	0.83	⋯	6.07	29
	⋯	⋯	⋯	±1.9	⋯	⋯	⋯	±1.2	±0.09	⋯	⋯	⋯
31015	34.4144	95.3	−53.16	44.0	0.364	60	55558.35	19.38	1.081	0.952	0.62	16
	±0.0008	⋯	±0.16	±0.4	±0.009	±1	±0.07	±0.13	±0.023	±0.011	⋯	⋯
	⋯	⋯	⋯	46.2	⋯	⋯	⋯	20.36	1.029	⋯	1.09	16
	⋯	⋯	⋯	±0.5	⋯	⋯	⋯	±0.20	±0.018	⋯	⋯	⋯
32012	89.49	30.3	−55.3	36.4	0.573	99	57120.5	36.8	1.16	0.92	1.46	19
	±0.01	⋯	±0.3	±0.8	±0.010	±3	±0.4	±0.7	±0.08	±0.03	⋯	⋯
	⋯	⋯	⋯	39.4	⋯	⋯	⋯	39.8	1.07	⋯	2.66	19

Table 7
(Continued)

ID	P (days)	Orbital Cycles	γ (km s^{-1})	K (km s^{-1})	e	ω (deg)	$T_\circ$ (HJD-2,400,000 days)	$a \sin i$ (10^6 km)	$m \sin^3 i$ ($M_\odot$)	q	σ (km s^{-1})	N
	...	...	...	±1.1	...	...	...	±1.1	±0.06	...	...	...
34016	18.17561	276.7	−54.92	50.77	0.351	205.8	55639.781	11.88	1.013	0.895	0.25	14
	±0.00007	...	±0.08	±0.11	±0.002	±0.5	±0.018	±0.03	±0.013	±0.006	...	...
	...	...	...	56.72	...	...	...	13.27	0.907	...	0.84	14
	...	...	...	±0.30	...	...	...	±0.08	±0.007	...	...	...
35019	18.6780	125.8	−52.6	48.6	0.200	52	56098.16	12.24	1.5	0.767	1.39	14
	±0.0019	...	±0.4	±0.6	±0.011	±3	±0.16	±0.17	±0.1	±0.024	...	...
	...	...	...	63.5	...	...	...	16.0	1.11	...	4.12	14
	...	...	...	±1.6	...	...	...	±0.5	±0.05	...	...	...
35021	22.03877	96.5	−54.4	47.90	0.257	44	56601.18	14.03	1.33	0.828	0.52	12
	±0.0007	...	±0.2	±0.21	±0.005	±1	±0.08	±0.07	±0.03	±0.009	...	...
	...	...	...	57.8	...	...	...	16.94	1.104	...	1.41	12
	...	...	...	±0.5	...	...	...	±0.18	±0.018	...	...	...
37008	2.498732	1751.3	−53.64	64.00	0.021	24	54975.3	2.199	0.599	0.685	1.30	22
	±0.000006	...	±0.32	±0.36	±0.008	±15	±0.1	±0.014	±0.015	±0.009	...	...
	...	...	...	93.43	...	...	...	3.21	0.410	...	3.53	22
	...	...	...	±0.95	...	...	...	±0.04	±0.007	...	...	...
40008	27.9376	179.9	−53.2	46.8	0.290	128	55230.1	17.22	1.364	0.876	2.08	33
	±0.0012	...	±0.2	±0.5	±0.006	±2	±0.1	±0.18	±0.025	±0.011	...	...
	...	...	...	53.4	...	...	...	19.65	1.20	...	1.65	33
	...	...	...	±0.4	...	...	...	±0.15	±0.03	...	...	...

(This table is available in machine-readable form.)

Table 8
NGC 7789 Photometric Variables

WOCS ID	Orbital Period (days)	Jahn et al. (1995)			Mochejska & Kaluzny (1999)			Zhang et al. (2003)			P_μ (%)	Comments
		ID	Type	Period (days)	ID	Type	Period (days)	ID	Type	Period (days)		
7029	...	...	...	...	...	...	...	v12	EW	0.3917	0	VRR, NM
11016	2.27414[a]	...	...	...	V39	EA	2.1077	...	...	...	0	BNM, SB1, RR
13004	...	V1	EW	1.19	V1	EW	1.1614	v1	...	...	100	BU, RR
14014	2.36601	...	...	...	V37	EA	1.2007	v10	...	...	96	BM, SB2
17028	3.553964	...	...	...	...	...	...	v30	EA	...	100	BM, SB2
20007	...	V13	...	...	...	...	...	...	...	...	98	BU
25008	...	V10	δ Scu	0.0955	V10	δ Scu	0.0868	...	...	...	81	SM, RR, BSS Member
33005	...	V2	EW	0.72	V2	EB	0.7165	...	...	...	97	VRR, M
33010	...	V6	EW	0.884	...	...	...	...	...	...	0	SNM

Notes. EA: β Persei type (semi-detached), EB: β Lyrae type (detached), EW: W Ursae Majoris type (contact).
[a] While this binary is considered a field star, we have a complete orbital solution for it and provide its parameters as follows: $P = 2.27414 \pm 0.00003$ days, $\gamma = -56.5 \pm 0.4$ km s^{-1}, $K = 17.5 \pm 0.5$ km s^{-1}, $e = 0.07 \pm 0.03$, $\omega = 90 \pm 30$ deg, $T_\circ = 55596.82 \pm 0.16$, $a \sin i = (0.547 \pm 0.015) \times 10^6$ km, $f(m) = 1.26\mathrm{e} - 3 \pm 0.11\mathrm{e} - 3\ M_\odot$, and $\sigma = 1.598$ km s^{-1}, $N = 23$.

The CPs of NGC 6819 and NGC 7789 do not evidently follow the same trend with age as the other binary populations (acknowledging the Hyades and Praesepe CP as an outlier).

The binaries defining the CPs in both of these clusters are different from the other populations in two important ways. First, the primary stars of these binaries have evolved off the cluster ZAMS. Tidal circularization rates increase sensitively with larger stellar radius. Second, the turnoff masses in NGC 6819 and NGC 7789 are 1.4 $M_\odot$ and 1.8 $M_\odot$, respectively. The primary stars of the binaries determining the CPs of these two clusters therefore have higher masses than the solar-like primary stars of the other binary populations. The more massive primary stars had at most only thin convective envelopes during most of their lifetimes prior to evolving off

the ZAMS. Tidal circularization rates are thought to decrease with less depth of outer convective zones.

Thus it is perhaps not a surprise that the CPs in these clusters are not consistent with the other populations. What is less clear is whether theory would predict the turnoff stars in NGC 6819 and NGC 7789 to have larger or smaller CPs. That work remains to be done.

In addition, future observational studies of NGC 7789 should probe further down the main sequence to determine the CP for binaries closer to solar mass.

11. Blue Stragglers

We define BSSs as being cluster members to the blue of the dashed line in Figure 17, which we place based on single-star and
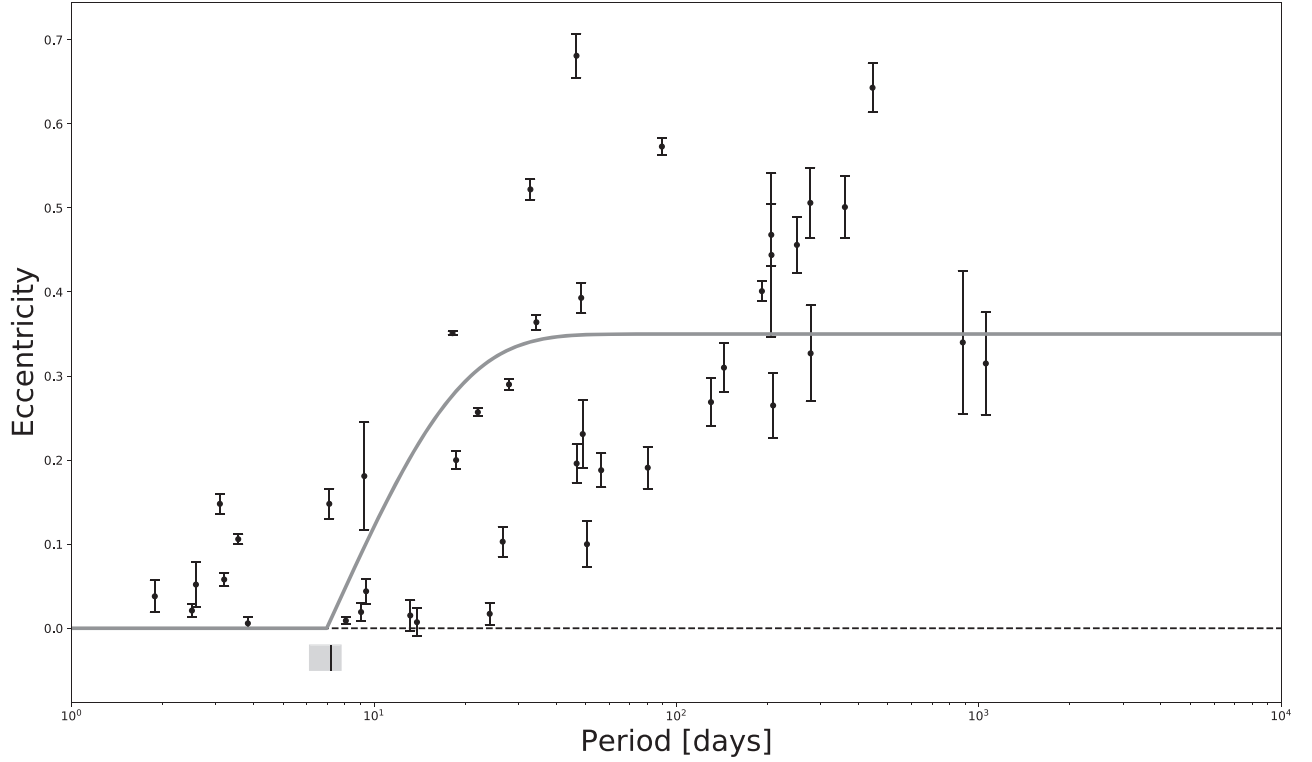
Figure 14. Orbital eccentricity vs. the orbital period for the main-sequence binaries in NGC 7789. The large eccentricities for long-period systems transition to circular orbits for short-period binaries. We determine the circularization period to be $7.2^{+0.6}_{-1.1}$ days indicated by a black dash near the bottom of the plot, with the uncertainty overplotted as a light gray bar. We also overplot the best-fit circularization function of Meibom & Mathieu (2005) in gray.
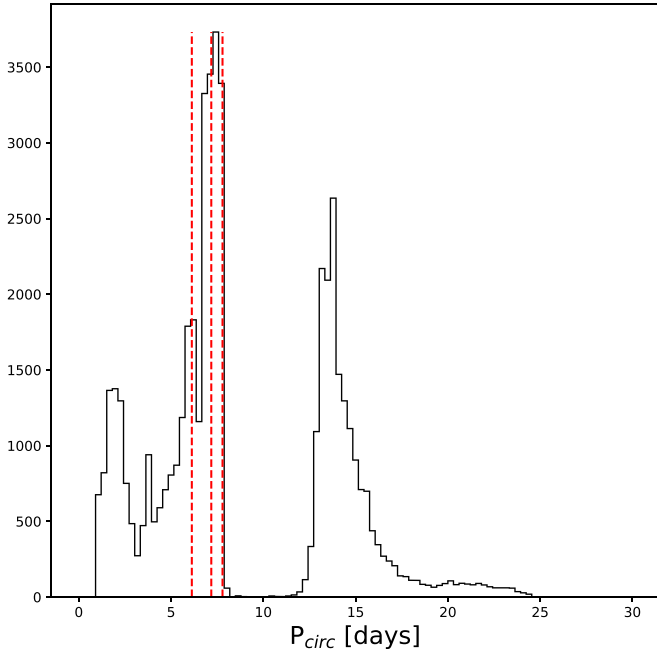

Figure 15. Distribution of trials produced by a bootstrap approach to measuring CP. The center red dashed line indicates the median of the shorter period peak (7.2 days), and the associated upper and lower lines represent the confidence intervals (+0.6 days, −1.1 days) containing 68% of trials around the median. Note an alternative possible CP of ∼14 days.

equal-mass binary isochrones. For reference, the ZAMS location of a 3.6 $M_\odot$ member, twice the turnoff mass of NGC 7789, is $G \sim 12.3$. This is very similar to the brightest BSS. We list 12 BSSs in Table 9 along with the number of WIYN RV

measurements, Gaia DR2 photometry, P_{RV}, P_μ, our RV membership classifications, as well as any additional comments.

Ten BSSs are three-dimensional cluster members. One more BSS has $P_{RV} \geqslant 90\%$ but high-noise PM information. One other BSS has $P_\mu = 99\%$, but no RV measurements due to it being a VRR. Because of their scientific interest as BSSs, we include all 12 stars as BSS cluster members.

Four of the BSSs have completed orbital solutions: WOCS 5011, WOCS 10011, WOCS 20009, and WOCS 36011. All of these stars are SB1s. WOCS 5011 and WOCS 20009 are both long-period SB1s with periods of 2710d and 4190d, respectively. Such periods are consistent with mass transfer from asymptotic branch giants (e.g., Geller & Mathieu 2011 and Gosnell et al. 2019, albeit with less massive turnoffs).

WOCS 36011, on the other hand, has a shorter period of 217 days and a much higher eccentricity with $e \sim 0.74$. BSSs with periods on the order of 10^2 days are likely the result of mass transfer from an RGB star, as in the case of WOCS 5379 in the open cluster NGC 188 (Gosnell et al. 2015; Mathieu & Geller 2015; Gosnell et al. 2019; M. Sun et al. 2020, in preparation). Interestingly, the CMD location of WOCS 36011 in NGC 7789 relative to the ZAMS and main-sequence turnoff is very similar to that of WOCS 5379 in NGC 188 (although the primary star of WOCS 36011 is of higher mass).

Our analysis of the mass function of WOCS 36011 is inconclusive regarding the presence of a white dwarf companion from an RGB donor star, as we can only place a lower limit on the companion stellar mass of ∼0.05 $M_\odot$. The very high eccentricity may be challenging to a mass-transfer origin, and certainly to its modeling. This BSS, like its counterpart in NGC 188, is the subject of continued observation.
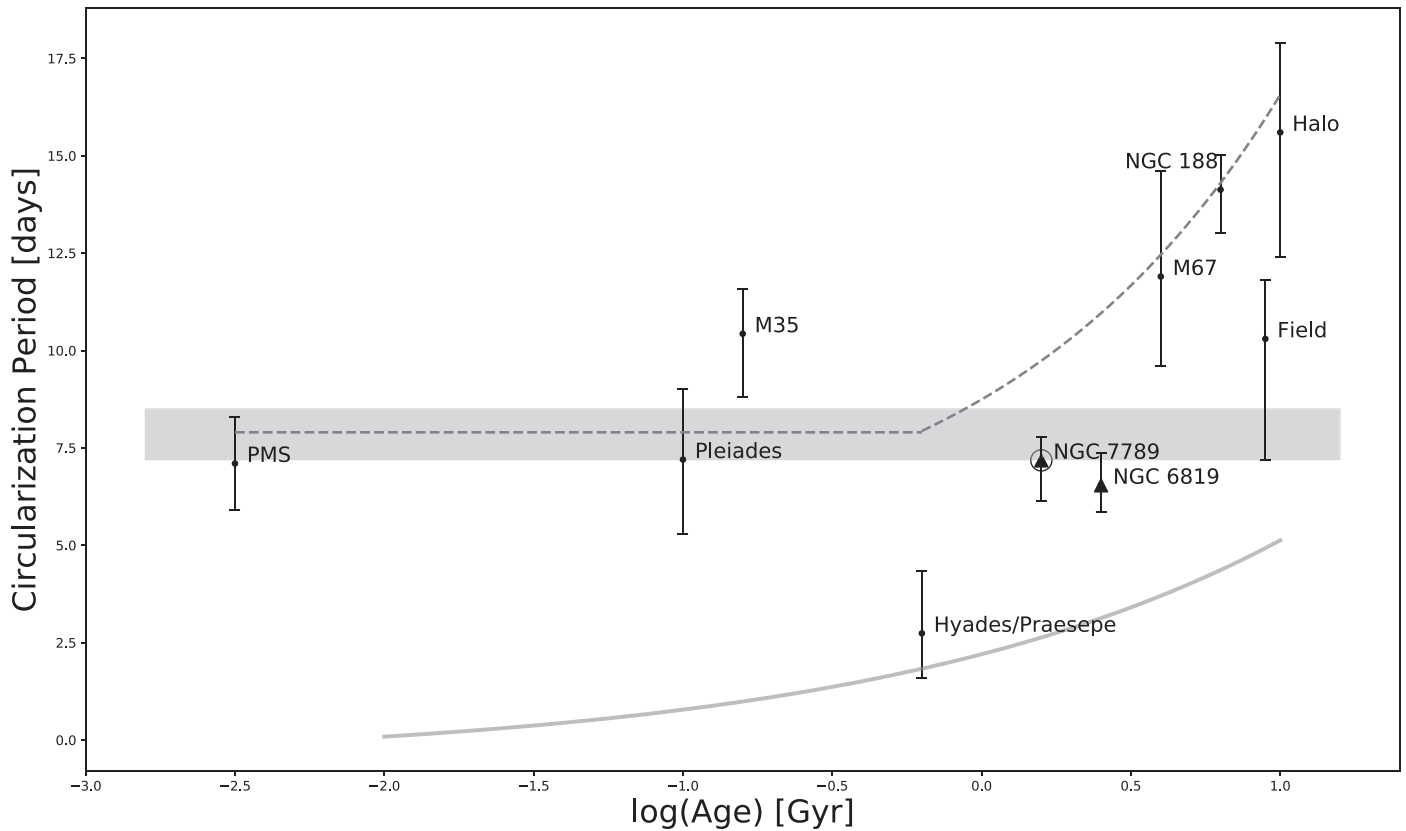
Figure 16. CP as a function of age for the eight populations of solar-like stars studied by Meibom & Mathieu (2005), with subsequent updated CP measurements for M35 and M67, a new measurement for NGC 6819, and our result for NGC 7789. The Zahn & Bouchet (1989) prediction for PMS tidal circularization is shown as the broad gray line. The BSE algorithm for main-sequence tidal circularization from Hurley et al. (2002) is shown as a gray line. Finally, the ad hoc tidal energy dissipation rate from Geller et al. (2013) is shown as the dashed line. NGC 7789 and NGC 6819 are marked with triangles since their CPs are derived using binaries with primary star masses of 1.4–1.8 $M_\odot$ that have evolved off the ZAMS.

WOCS 10011 has a similarly low period and substantial eccentricity, with a period of 517 days and $e \sim 0.37$. It may be the case that this binary is not a true BSS, but rather on the cluster blue hook. For the purposes of this work, we consider it to be a BSS candidate.

The orbital periods found so far for the NGC 7789 BSS are in line with the BSS orbital periods found for the intermediate-aged open cluster NGC 6819, where three SB1 BSSs with orbital solutions have periods of 762, 1144, and 3900 days (Milliman et al. 2014). These orbital periods are consistent with those of the rich population of BSSs in the much older open cluster NGC 188, where all but one of the SB1 BSSs (13/14) have periods on the order of 10^3 days (Geller & Mathieu 2012).

With the four detected velocity-variable BSSs we find a BSS binary frequency of $33 \pm 17\%$. This is consistent with the $40\% \pm 16\%$ found for NGC 6819 (Milliman et al. 2014) and substantially less than the $80\% \pm 20\%$ BSS binary fraction found for NGC 188 (Mathieu & Geller 2009) and the $79\% \pm 24\%$ BSS binary fraction found in M67 (Geller et al. 2015). We note that three of our BSS candidates lie close to our color cutoff: WOCS 10011, WOCS 25008, and WOCS 25024. If we exclude these borderline BSS candidates, the BSS binary frequency is then $33\% \pm 19\%$, still consistent with NGC 6819. Excluding also the other BSS candidate with rapid rotation, WOCS 3009, the binary frequency is then $38\% \pm 22\%$.

12. Summary

We present the results of a complete and extensive time-series RV survey of 1206 stars in the open cluster NGC 7789. The stellar sample extends to a radius of $\sim 18'$ (10 pc in projection) from the cluster center and covers a G mag range from ~ 10 to 15. This magnitude range includes evolved main-sequence stars to 1 mag below the turnoff, giants, red clump stars, BSSs, and SSG and RSS candidates.

We use these RV measurements and Gaia DR2 proper-motion data to derive a sample of 624 cluster members. We identify 102 velocity-variable cluster members, and present spectroscopic orbital solutions for 81 binaries. We calculate an incompleteness-corrected main-sequence binary fraction of $31\% \pm 4\%$ for binaries with periods under 10,000 days, consistent with other open clusters studied by WOCS. We find a tidal circularization period of $7.2^{+0.6}_{-1.1}$ days.

We detect $33\% \pm 17\%$ of BSSs as velocity variable, consistent with the frequency of velocity-variable BSSs in the similarly aged cluster NGC 6819. We also identify two BSSs, WOCS 10011 and WOCS 36011, whose low periods and significant eccentricities may be the result of mass transfer from an RGB star.

We also find one rapidly rotating SSG, a second SSG candidate, and one RSS candidate in our sample. We look forward to our expanded observations of NGC 7789 that will shed more light on these alternative stellar evolution products.
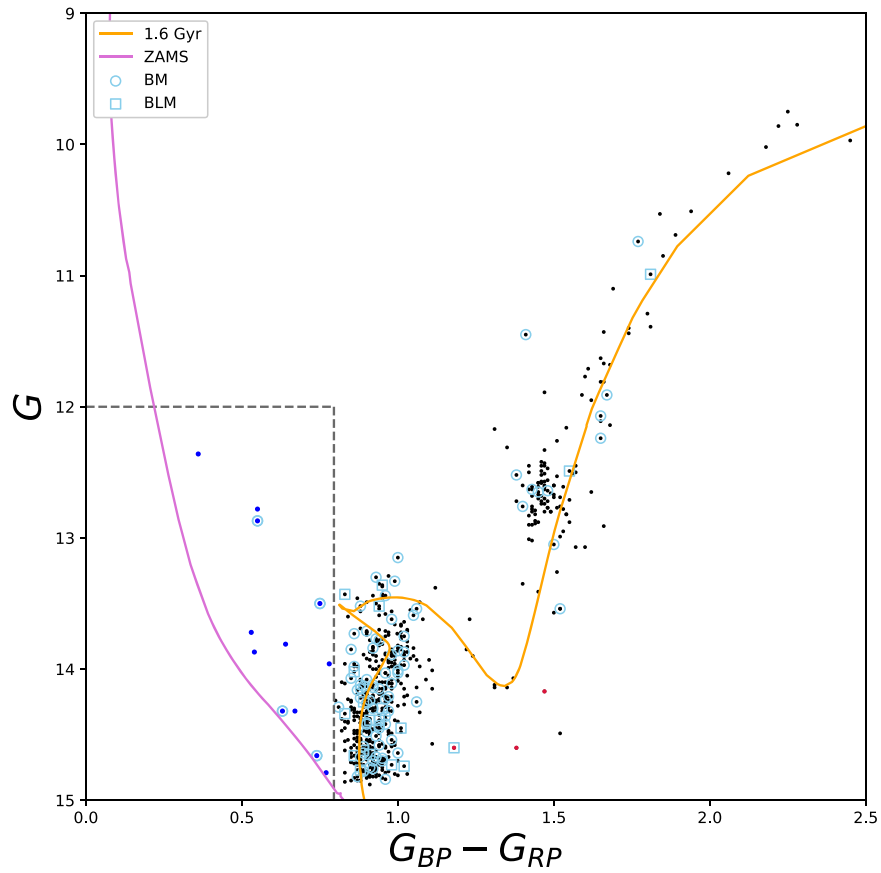
Figure 17. Same as Figure 11, but highlighting the BSSs (blue dots) that fall to the blue of the vertical dashed line. Binary BSSs, all of which have orbital solutions, are outlined with an additional blue circle. The brightest BSS is a VRR.

Table 9
NGC 7789 Blue Straggler Members

WOCS ID	N	G	$G_{BP} - G_{RP}$	P_{RV}	P_{μ}	Class	Comment
RV and PM Members:							
5004	14	12.78	0.55	95	99	SM	⋯
5011	34	12.87	0.55	95	99	BM	RR
10010	9	13.72	0.53	95	96	SM	⋯
15015	9	13.87	0.54	95	99	SM	⋯
16020	18	13.81	0.64	95	99	SM	⋯
20009	42	14.32	0.63	62	99	BM	⋯
25008[a]	13	13.96	0.78	94	81	SM	RR
25024[a]	11	14.79	0.77	94	99	SM	RR
27010	14	14.32	0.67	94	99	SM	⋯
36011	13	14.66	0.74	94	98	BM	⋯
RV Member with High-noise PM Information:							
10011[a]	22	13.50	0.75	96	⋯	BM	⋯
RV VRR and PM Member:							
3009	⋯	12.36	0.36	⋯	99	VRR, M	⋯

Note.
[a] These are the BSSs marked as borderline as discussed in Section 11 because of proximity to our color cutoff.

by national institutions, in particular the institutions participating in the Gaia Multilateral Agreement.

This work has also made use of Astropy (http://www.astropy.org), a community-developed core Python package for Astronomy (Astropy Collaboration et al. 2013, 2018), as well as dustmaps (Green 2018) and MATLAB (MATLAB 2019).

This work was conducted at the University of Wisconsin–Madison which is located on occupied ancestral land of the Ho-chunk Nation, and observations for this work were conducted on the traditional lands of the Tohono O'odham Nation. We respect the inherent sovereignty of these nations, along with the other 11 First Nations in Wisconsin as well as the southwestern tribes of Arizona. We honor with gratitude these lands and the peoples who have stewarded them, and who continue to steward them, throughout the generations.

ORCID iDs

Andrew C. Nine ⬡ https://orcid.org/0000-0002-6478-0611
Katelyn E. Milliman ⬡ https://orcid.org/0000-0002-8308-1998
Robert D. Mathieu ⬡ https://orcid.org/0000-0002-7130-2757
Aaron M. Geller ⬡ https://orcid.org/0000-0002-3881-9332
Emily M. Leiner ⬡ https://orcid.org/0000-0002-3944-8406
Imants Platais ⬡ https://orcid.org/0000-0003-2599-2459
Benjamin M. Tofflemire ⬡ https://orcid.org/0000-0003-2053-0749

References

Astropy Collaboration, Price-Whelan, A. M., Sipőcz, B. M., et al. 2018, AJ, 156, 123
Astropy Collaboration, Robitaille, T. P., Tollerud, E. J., et al. 2013, A&A, 558, A33
Barden, S. C., Armandroff, T., Muller, G., et al. 1994, Proc. SPIE, 2198, 87
Burbidge, E. M., & Sandage, A. 1958, ApJ, 128, 174
Cantat-Gaudin, T., Jordi, C., Vallenari, A., et al. 2018, A&A, 618, A93
Casamiquela, L., Carrera, R., Jordi, C., et al. 2016, MNRAS, 458, 3150
Deliyannis, C. P., Anthony-Twarog, B. J., Lee-Brown, D. B., & Twarog, B. A. 2019, AJ, 158, 163
Dotter, A. 2016, ApJS, 222, 8
Fletcher, J. M., Harris, H. C., McClure, R. D., & Scarfe, C. D. 1982, PASP, 94, 1017
Gaia Collaboration, Babusiaux, C., van Leeuwen, F., et al. 2018a, A&A, 616, A10
Gaia Collaboration, Brown, A. G. A., Vallenari, A., et al. 2018b, A&A, 616, A1
Gaia Collaboration, Prusti, T., de Bruijne, J. H. J., et al. 2016, A&A, 595, A1
Gao, X.-h. 2018, PASP, 130, 124101
Geller, A. M., Hurley, J. R., & Mathieu, R. D. 2013, AJ, 145, 8
Geller, A. M., Latham, D. W., & Mathieu, R. D. 2015, AJ, 150, 97
Geller, A. M., Leiner, E. M., Bellini, A., et al. 2017a, ApJ, 840, 66
Geller, A. M., Leiner, E. M., Chatterjee, S., et al. 2017b, ApJ, 842, 1
Geller, A. M., & Mathieu, R. D. 2011, Natur, 478, 356
Geller, A. M., & Mathieu, R. D. 2012, AJ, 144, 54
Geller, A. M., Mathieu, R. D., Braden, E. K., et al. 2010, AJ, 139, 1383
Geller, A. M., Mathieu, R. D., Harris, H. C., & McClure, R. D. 2008, AJ, 135, 2264
Gim, M., Hesser, J. E., McClure, R. D., & Stetson, P. B. 1998a, PASP, 110, 1172
Gim, M., Vandenberg, D. A., Stetson, P. B., Hesser, J. E., & Zurek, D. R. 1998b, PASP, 110, 1318
Gosnell, N. M., Leiner, E. M., Mathieu, R. D., et al. 2019, ApJ, 885, 45
Gosnell, N. M., Mathieu, R. D., Geller, A. M., et al. 2015, ApJ, 814, 163
Green, G. 2018, JOSS, 3, 695
Green, G. M., Schlafly, E., Zucker, C., Speagle, J. S., & Finkbeiner, D. 2019, ApJ, 887, 93
Hurley, J. R., Tout, C. A., & Pols, O. R. 2002, MNRAS, 329, 897
Jacobson, H. R., Pilachowski, C. A., & Friel, E. D. 2011, AJ, 142, 59
Jahn, K., Kaluzny, J., & Rucinski, S. M. 1995, A&A, 295, 101
Kroupa, P. 1995, MNRAS, 277, 1507
Kurucz, R. L. 1993, in Light Curve Modeling of Eclipsing Binary Stars, ed. E. F. Milone (Berlin: Springer), 93
Latham, D. W., Stefanik, R. P., & Carney, B. W. 1985, in Stellar Radial Velocities, ed. A. G. D. Philip & D. W. Latham (Schenectady, NY: L. Davis Press), 381
Leiner, E., Mathieu, R. D., & Geller, A. M. 2017, ApJ, 840, 67
Leiner, E., Mathieu, R. D., Vanderburg, A., Gosnell, N. M., & Smith, J. C. 2019, ApJ, 881, 47
Leiner, E. M., Mathieu, R. D., Gosnell, N. M., & Geller, A. M. 2015, AJ, 150, 10
Mathieu, R. D. 1983, ApJL, 267, L97
Mathieu, R. D. 2000, ASP Conf. Ser. 198, Stellar Clusters and Associations: Convection, Rotation, and Dynamos, ed. R. Pallavicini, G. Micela, & S. Sciortino (San Francisco, CA: ASP), 517
Mathieu, R. D., & Geller, A. M. 2009, Natur, 462, 1032
Mathieu, R. D., & Geller, A. M. 2015, in Astrophysics and Space Science Library, Vol. 413, Ecology of Blue Straggler Stars, ed. H. M. J. Boffin, G. Carraro, & G. Beccari (Berlin: Springer), 29
Mathieu, R. D., & Leiner, E. M. 2019, The Impact of Binary Stars on Stellar Evolution, Cambridge Astrophysics (Cambridge: Cambridge Univ. Press), 261
MATLAB 2019, MATLAB version 9.6 (R2019a) (Natick, MA: The Mathworks, Inc.)
McNamara, B. J., & Solomon, S. 1981, A&AS, 43, 337
Meibom, S., Barnes, S. A., Platais, I., et al. 2015, Natur, 517, 589
Meibom, S., Grundahl, F., Clausen, J. V., et al. 2009, AJ, 137, 5086
Meibom, S., & Mathieu, R. D. 2005, ApJ, 620, 970
Milliman, K. E., Leiner, E., Mathieu, R. D., Tofflemire, B. M., & Platais, I. 2016, AJ, 151, 152
Milliman, K. E., Mathieu, R. D., Geller, A. M., et al. 2014, AJ, 148, 38
Milliman, K. E., Mathieu, R. D., & Schuler, S. C. 2015, AJ, 150, 84
Mochejska, B. J., & Kaluzny, J. 1999, AcA, 49, 351
Overbeek, J. C., Friel, E. D., Jacobson, H. R., et al. 2015, AJ, 149, 15
Pancino, E., Carrera, R., Rossetti, E., & Gallart, C. 2010, A&A, 511, A56
Platais, I., Gosnell, N. M., Meibom, S., et al. 2013, AJ, 146, 43
Platais, I., Kozhurina-Platais, V., Mathieu, R. D., Girard, T. M., & van Altena, W. F. 2003, AJ, 126, 2922
Raghavan, D., McAlister, H. A., Henry, T. J., et al. 2010, ApJS, 190, 1
Sandquist, E. L., Mathieu, R. D., Quinn, S. N., et al. 2018, AJ, 155, 152
Sarajedini, A., von Hippel, T., Kozhurina-Platais, V., & Demarque, P. 1999, AJ, 118, 2894
Taylor, M. B. 2005, in ASP Conf. Ser. 347, Astronomical Data Analysis Software and Systems XIV, ed. P. Shopbell, M. Britton, & R. Ebert (San Francisco, CA: ASP), 29
Thompson, B., Frinchaboy, P., Kinemuchi, K., Sarajedini, A., & Cohen, R. 2014, AJ, 148, 85
Tofflemire, B. M., Gosnell, N. M., Mathieu, R. D., & Platais, I. 2014, AJ, 148, 61
van Dokkum, P. G. 2001, PASP, 113, 1420
Wu, Z.-Y., Du, C.-H., Ma, J., & Zhou, X. 2009, ChPhL, 26, 029701
Wu, Z.-Y., Zhou, X., Ma, J., et al. 2007, AJ, 133, 2061
Yang, S.-C., Sarajedini, A., Deliyannis, C. P., et al. 2013, ApJ, 762, 3
Zahn, J.-P., & Bouchet, L. 1989, A&A, 223, 112
Zhang, X.-B., Deng, L.-C., Xin, Y., & Zhou, X. 2003, ChJAA, 3, 151
Zucker, S., & Mazeh, T. 1994, ApJ, 420, 806